FRONT MATTER

Title

Amoeboid cells undergo durotaxis with soft end polarized NMIIA

Authors

Xin Yi[1, 2, 3#], Pengcheng Chen[4#], Chenlu Kang[1,2,3#], Dong Li[5, 7], Yihong Yang[5,6], Huaqing Cai[5, 6], Bo Li[4*], Congying Wu[1, 2, 3*]

Affiliations

1: Institute of Systems Biomedicine, School of Basic Medical Sciences, Peking University Health Science Center, Beijing, 100191 China;

2: Beijing Key Laboratory of Tumor Systems Biology, Peking University Health Science Center, Beijing, 100191 China;

3: International Cancer Institute, Peking University, Beijing, 100191 China;

4: Institute of Biomechanics and Medical Engineering, Applied Mechanics Laboratory, Department of Engineering Mechanics, Tsinghua University, Beijing, 100084, China.

5: National Laboratory of Biomacromolecules, Institute of Biophysics, Chinese Academy of Sciences, 100101 Beijing, China.

6: College of Life Sciences, University of Chinese Academy of Sciences, 100049 Beijing, China.

7: School of Life Sciences and Medicine, University of Science and Technology of China, 230027 Hefei, China.

Abstract

Cell migration towards stiff substrates has been coined as durotaxis and implicated in development, wound healing and cancer, where complex interplays between immune and non-immune cells are present. Compared to the emerging mechanisms underlying the strongly adhesive mesenchymal durotaxis, little is known about whether immune cells - migrating in amoeboid mode - could follow mechanical cues. Here we develop an imaging-based confined migration device that provides stiffness gradient for cell migration. By tracking live cell trajectory and analyzing the directionality T cells and neutrophils, we observe that amoeboid cells can durotax. We further delineate the underlying mechanism to involve non-muscle myosin IIA (NMIIA) polarization towards the soft-matrix-side but may not require differential actin flow up- or down-stiffness gradient. Using the protista *Dictyostelium*, we further demonstrate the evolutionary conservation of amoeboid durotaxis. Finally, these experimental phenomena are theoretically captured by an active gel model capable of mechanosensing. Collectively,

these results may shed new lights on immune surveillance and recently identified confined migration of cancer cells, within the tumor microenvironment or the inflamed fibrotic tissues.

KEY WORDS

cell migration, cytoskeleton, T cell, neutrophil, mechanobiology, active gel modeling, gradient gel.

MAIN TEXT

Introduction

Cell migration is essential to myriads of physiological and pathological processes including cancer dissemination (1). As the mechanical properties of tumor microenvironment being gradually unveiled , waves of studies have focused on the contribution of mechanical force - in the forms of proliferation generated cell jamming (2) and fibrosis induced tissue stiffening - on tumor expansion as well as invasion (3). The ability of cells to sense and navigate along higher substrate stiffness has been coined as “durotaxis” in the early 2000s (4) with important pathophysiological implications (5). Over the past two decades, accumulating in vitro and in vivo evidence has demonstrated durotaxis in tumor epithelial sheets and single mesenchymal cells (6-9), and revealed mechanisms including focal adhesion tugging or probing of the local substrate by actin-based protrusions to underlie this specialized directional cell migration (6, 10-12). However, compared to tumor cells that harness the capacity to durotax, little is known about whether microenvironmental stiffness difference could determine the destination of immune cells.

In contrast to mesenchymal migration adopted by some tumor cells, immune cells mainly undergo rapid single cell crawling referred to as ‘amoeboid’ migration, without formation of stable focal adhesions but can achieve migration ten times faster (13). Modeling on amoeboid migration suggested that myosin contractility may play an important role when mechanical anchoring are less evident (14). In this model, actomyosin was described as an active gel whose polarity dictates the alignment of actin fibers (14). Moreover, in silicon simulation suggested that actomyosin contractility can lead to collective internal flows of actin, which, in turn, propels the cell body forward (15). Meanwhile, experiments have also revealed that protrusive flowing of the anterior actin network drives the adhesion-independent cell migration.

During development and immune surveillance, chemotactic cues have been reported to globally prescribe the migratory direction and destination of immune cells (16). Using

mammalian leukocytes and lymphocytes (17, 18) as well as the protista *Dictyostelium* (19), mechanisms of amoeboid chemotaxis have been extensively studied . Instead, little is known about how these cells respond to mechanical cues and whether they would undergo durotactic migration. Previous studies have shown that inflamed, stiffened endothelial cells could induce more neutrophil transmigration (20), and that once adhered to the endothelium, transmigrating neutrophils may exert durotactic sensing to search for stiffer sites (21). In addition, lymphocytes such as $CD4^+$ Naïve T cells increased spreading area when plated on stiffer substrates (22), indicative of the capacity to sense external mechanical signal. The above evidence argued that amoeboid cells, albeit with no strong adhesions, were able to sense and respond to environmental stiffness.

Here we developed an imaging-based cell migration device that provided both spatial confinement and stiffness gradient. By tracking live cell trajectory and analyzing the directionality T cells and neutrophils, we observed that amoeboid cells can durotax. We further uncovered the underlying mechanism to be NMII (non-muscle myosin II) dependent. Based on our observations that NMIIA was polarized towards the soft-end in cells on stiffness gradient gel, we established a mechanical model simulating amoeboid cells as active droplets, predicting that durotaxis can be strengthened on the softer region of the gradient substrate which was then verified experimentally. Moreover, we demonstrated the evolutionarily conservation of amoeboid migration in the protista *Dictyostelium*. Together, the identification that rigidity-guided migration existed in low-adhesive, fast moving amoeboid cells may provide new insights in focal adhesion-independent mechanosensing, and may shed new lights on immune surveillance and cancer metastasis.

Results

Result 1 T cells and neutrophils undergo durotactic migration

T cells and neutrophils exert amoeboid migration in vivo and in vitro under confinement (23, 24). To probe whether amoeboid cells would undergo durotaxis, we manufactured an imaging-based cell migration device which provided spatial confinement to maintain amoeboid cell migration (23, 25) and stiffness gradient to provide durotactic cue. Typically, cells were sandwiched between polyacrylamide (PA) gel with gradient (Fig. S1A, 20.77 kPa/mm; see Methods) or uniform stiffness (26) and a thin agarose patch (Fig. 1A iv-vii). Cell migration trajectories from time-lapse imaging were then generated and analyzed for directionality. We employed the Forward Migration Index (FMI), for which the displacement value was divided by

the total displacement the cell underwent (Fig. 1B) (7, 18, 26, 27). This FMI is decoupled with cell velocity and differed from persistence. As FMI increased, cell persistence could be decreased (Fig. S2A), unchanged (Fig. S2B) or increased (Fig. S2C).

We then performed time-lapse imaging to record $CD4^+$ Naïve T cell motility and generated trajectories for direction analysis. As reported previously (13), we observed that T cells underwent typical amoeboid migration with relatively high speed (the mean velocity was 7.23 μm/min) (Fig. 1C, F, Movie 1, 2), distinguished from mesenchymal migration which is usually below 1 μm/min (28). When we stained these T cells for focal adhesion marker paxillin (27), we detected puncta-like signals (Fig. S1B), distinguished from the plaque-like structure in mesenchymal cells such as the MDA-MB 231 (Fig. S1C).

The trajectories of T cells on the uniform gel did not show biased direction (Fig. 1C-E, Movie 1), while in striking contrast, a majority of cells on the gradient gel exhibited inclined movement towards the stiff-end (Fig. 1C-E, Movie 2). FMI for cells on the uniform gel was around zero (indicating random motility) (Fig. 1F), while it displayed a positive value for cells on the stiffness gradient gel and significantly exceeded that of cells on the uniform gel (Fig. 1F). Angular displacement comparison also revealed that T cells migrated towards the stiff end in this experimental setting (Fig. 1E). Besides, no obvious difference in velocity was detected when comparing T cells moving on uniform vs gradient gel (Fig. 1F), indicating that stiff gradient did not enhance motility but rather increases forward migratory steps.

Having identified durotaxis in T cells, we next sought to evaluate in other amoeboid cells such as neutrophils whether they also possess the durotactic capacity. Bone marrow-derived neutrophils were isolated by Percoll gradient and confined between the stiffness gradient gel and the agarose block. In line with our observations with T cells, neutrophils displayed random gliding on the uniform gel while appeared to durotax on the gradient gel, as revealed by the FMI and angular displacement analysis (Fig. 1G-J, Movie 3). This prominent stiff-end directed movement may result from (1) initial cell polarization upon seeding, exemplified by subsequent persistent migration towards the cell front; or (2) cells frequently exploring and re-steering to the stiffer side of the substrate. When analyzing live cell trajectories, we found that some cells indeed exhibited highly persistent migration (Fig. S1C, Track 2, 3, 5, 9, Movie 4). However, we again detected cells that frequently changed directions but showed stiff-end biased migration on the whole (Fig. S1C, Track 1, 4, 6, 7, 8, Movie 4). These observations indicated that neutrophils were able to sense stiffness difference and re-polarize to durotax. Analysis of the bulk cell population revealed that neutrophils on stiffness gradient gel did not elevate their persistence compared to those on the uniform gel (Fig. 1J). Since symmetrical migratory paths can have the same

persistence value with different FMI (Fig. S2B), the observation that cells can enhance the FMI without persistence increase can be explained by more frequent forward migratory events. These results preclude that neutrophil durotaxis is simply resulted from biased initial adhesion and spreading towards the stiff end. We also employed an immortalized promyelocytic leukemia cell line HL-60 in addition to the mouse derived neutrophils. In agreement with previous reports, we detected that HL-60 employs amoeboid migration when differentiated into neutrophil-like cells (dHL-60) (29) (Fig. 1K, Fig. S3A, Movie 5). dHL-60 cells migrated randomly on the uniform gel while moved towards the stiff end on gradient gel (Fig. 1K-N, Movie 5) under confinement.

Together, these phenomena indicate that amoeboid cells such as T cells and neutrophils, although lacking stable focal adhesions, are capable to sense the stiffness gradient and orchestrate directional migration towards the stiffer side.

Result 2 Amoeboid durotaxis may not be propelled by differential actin flow

Having observed that amoeboid cells can exert durotactic migration, we then interrogated the molecular underpinnings. Classic molecular clutch model attributed both single and collective mesenchymal durotaxis to the differential adhesion strength on distinct substrate stiffness (10, 12, 30). Enhanced traction strain energy on stiffer matrix (30, 31) indicates the presence of increased motors and clutches, which may then slow down the actin flow at adhesion sites by friction (30). In this sense, actin flow is mechanosensitive – with low speed on stiff substrate and high speed on soft matrix. To test the rigidity sensitivity of actin flow in amoeboid cells, we performed quantitative fluorescent speckle microscopy (qFSM) to monitor fluorescent particle movement in dHL-60 cells stained with the actin-specific dye SiR-Actin. Retrograde flow analysis (32) revealed that actin flow velocity dropped sharply when cells were plated on stiffer substrate (160 kPa) compared to the soft gel (4 kPa) (Fig. 2A, Movie 6,7). Moreover, a descending trend of actin flow speed was detected with increasing substrate stiffness (Fig.2A, Movie 6-10), suggesting that actin flow in amoeboid cells can indeed respond to stiffness.

Actin flow is generated by monomer assembly at the leading edge and myosin contraction at the cell rear, while is slowed down by traction stress between the cell bottom and the substrate (33). Strain energy from the halting of actin flow then transduces into protruding force to counteract membrane tension at the cell front (23, 34). Thus, the protrusion rate is inversely related to the actin retrograde flow (35). It has been suggested that continuous cycles of protrusion support forward cell migration (36). Considering the negatively correlated actin flow speed and substrate stiffness (Fig. 2A), we postulated that differential actin flow velocity (high speed in the down-gradient vs low speed in the up-gradient region) may promote stiff end biased

cell migration by inducing more protrusive events in the up-gradient cell region. To test this, we divided the cell body area into up- and down-gradient halves for respective actin flow analysis. However, against our hypothesis, actin flow in these two regions appeared similar in speed (Fig. 2B, Movie 11). This phenomenon argues against differential actin flow playing a crucial role in amoeboid durotaxis.

Result 3 Durotaxis of T cells and neutrophils is regulated by polarized actomyosin activity

Current mechanistic models explaining directional cell migration along or against a stiffness gradient such as focal adhesion tugging or probing of the local substrate by actin-based protrusions (10-12) in mesenchymal cells are not plausible in the setting of amoeboid cells due to the lack of focal adhesions. The microtubule dynamics has been reported to impact amoeboid migration (37). Besides, we previously found that perturbation of the microtubule network - especially loss of the Golgi microtubules - abrogated single cell durotaxis in HRPE cells (26). However, no obvious alterations in durotactic FMI were detected under treatments of either the microtubule polymerization inhibitor Nocodazole or the depolymerization inhibitor Taxol (26, 38), indicating that similar influence of the microtubule network on mesenchymal cells may not apply to amoeboid durotaxis (Fig. 2C).

Recently, the cell rear-localized actomyosin network has been inferred to determine polarity re-establishment by mediating contractility underneath the plasma membrane and propels the locomotion of the cell body. We then asked whether this machinery could provide steering force for focal adhesion-independent durotaxis. Interestingly, treating T cells or neutrophils with the NMII inhibitor blebbistatin to disrupt cell contraction drastically reduced durotactic FMI towards zero (Fig. 2D, E; Movie 12). In contrast, Rho activator II, which can enhance myosin contractility, elevated the FMI of durotactic T cells and neutrophils (Fig. 2D, E), supporting the notion that NMII activation may play an important role in amoeboid durotaxis. Pharmacological perturbations in dHL-60 cells with blebbistatin or Rho activator II showed similar effects with what we observed in T cells (Fig. 2D, F), agreeing with myosin activity being pivotal for amoeboid durotaxis.

It has been documented that NMIIB is more sensitive to stiffness gradient than NMIIA in mesenchymal stem cells (6). Having observed that NMII inhibition significantly decreased FMI in T cells and neutrophils, we next set to explore the roles of specific NMII isoforms in amoeboid durotaxis. We generated HL-60 cells knocked down of NMIIA or NMIIB (Fig. 3A, Fig. S4A). Interestingly, cell trajectories on gradient gel revealed that loss of NMIIA rather than NMIIB abolished dHL-60 durotaxis (Fig. 3B-E, Movie 13), which was not in accordance with what has

been reported in mesenchymal cells (39).

Previous studies showed that when mesenchymal cells crawl on rigid glass, NMIIB is enriched at the cell rear (40), whereas NMIIA appears uniformly distributed (6). To examine the mechanism underlying the requirement for NMIIA but not NMIIB in amoeboid durotaxis, we assayed their distribution in cells on gradient gel. Strikingly, NMIIA was concentrated at the down-gradient side of the HL-60 cells, regardless of the front-rear axis of the cell (Fig. 3F, G). On the contrary, NMIIB exclusively localized at the cell front, with much less correlation with the stiffness gradient (Fig. 3G), consistent with it playing a minor role in the establishment of durotactic direction. Similar distribution of NMIIA was also seen in T cells and neutrophils on gradient gel (Fig. 3H, Fig. S4B, C).

Previous studies suggested that localizing NMIIA to the cell rear is required to set cell polarity (6, 41). We then hypothesized that the down-gradient concentrated NMIIA may leverage the cell front towards the stiffer side, thus enabling efficient amoeboid durotaxis. To test this, we transfected HL-60 cells with GFP-NMIIA and monitored the fluorescent signal in durotaxis assays. We captured events when cells turned to align with the stiffness gradient and in these cases, the GFP-NMIIA signal stayed concentrated at the soft side, preceding re-polarization of the cell to form a new front-rear axis (Fig. S5A, Movie 14).

Result 4 Amoeboid durotaxis is evolutionarily conserved

Having identified durotactic behavior in T cells and neutrophils, we then asked whether this low-adhesive, rapid moving durotaxis was evolutionarily conserved. To answer this, we switched to the protista *Dictyostelium*, which move in amoeboid mode when reside as single cells. After being plated on PA gel surface under confinement, *Dictyostelium* exhibited elongated morphology and extended convex membrane protrusions at the front as described before (42), which then alternated sideways for gliding (Fig. 4A, Movie 15). Agreeing with our previous findings with T cells and neutrophils, *Dictyostelium* also displayed stiff-side directed motility when seeded on the gradient gel (Fig. 4A-D, Movie 15). Blebbistatin application drastically dropped the durotactic FMI to around zero (Fig. 4E), while Rho activator II treatment significantly elevated this value (Fig. 4E). Moreover, in line with what we discovered in T cells, microtubule perturbation did not hamper the directionality of *Dictyostelium* durotaxis (Fig. 4F). These results suggest that the molecular mechanism underlying amoeboid durotaxis is largely conserved in *Dictyostelium* (Fig. 4E & Fig. 2C, D).

Result 5 Mechanosensing active gel model captures amoeboid durotaxis

To better characterize amoeboid durotaxis observed in our experiments, we establish an active gel model (15), in which a cell is represented by an active droplet (Fig 5A) $c(\mathbf{r},t)$ composed of actin filaments with a certain density , whose polarization field is defined by $\mathbf{P}(\mathbf{r},t)$ (Fig. 5B), with $\mathbf{r}$ and t denoting the position vector and time, respectively. The free energy $F[c,\mathbf{P}]$ to confine actin assembly into a droplet can be formulated as (15):

$$F[c,\mathbf{P}] = \int d^3r \left\{ \frac{4a}{c_0^4} c^2 (c-c_0)^2 + \frac{k}{2}|\nabla c|^2 - \frac{\alpha}{2}\frac{(2c-c_0)}{c_0}|\mathbf{P}|^2 + \frac{\alpha}{4}|\mathbf{P}|^4 + \frac{\kappa}{2}(\nabla \mathbf{P})^2 \right\}. \quad (1)$$

This energy ensured that a polar active actin phase $c>c_0$ ($|\mathbf{P}|>0$) and a passive solvent phase c=0 ($|\mathbf{P}|$=0) coexist in this system, where c_0 denotes the average actin density. α is the stability constant and k determines the interfacial tension between actin and adjacent solvent phase. a is a phenomenological free energy amplitude to define the bulk property of the droplet, and κ describes the elastic constant of liquid-crystalline elasticity. In addition, fluid velocity $\mathbf{v}$, which is involved in actin convection, is incorporated here. Cell migration is described by the spatial evolution of actin density $c(\mathbf{r},t)$ and can be influenced by the fluid velocity and polarization field. The active contraction of cells is represented by the active stress $\boldsymbol{\sigma}^{\mathrm{act}} = \bar{\zeta} c \mathbf{P}\mathbf{P}$, where $\bar{\zeta}$ measures the contractile strength. NMIIA is related to cell polarity establishment during cell durotaxis (6). In our amoeboid durotaxis experiments, we observed soft-end polarized NMIIA (Fig. S5A), which is involved in the present model. Thus, we propose that the density of NMIIA m evolves as:

$$\frac{\partial m}{\partial t} + \nabla \cdot \left[m(\mathbf{v} - w\mathbf{P}) \right] = \mathrm{D}_m(E) \nabla \cdot \nabla m - \frac{1}{\Gamma_m}\left[-\mathrm{sign}(2c-c_0)\alpha m + \alpha \frac{m^3}{m_0^2} \right] \quad (2),$$

where $\mathrm{D}_m(E)$ denotes diffusive ability of NMIIA and is related to the substrate stiffness E. The diffusion parameter $\mathrm{D}_m(E)$ outside the cell ($c<c_0/2$) is set to be uniform and defined by the basal diffusion parameter D_0. Inside the cell, $\mathrm{D}_m(E)$ is defined by

$$\mathrm{D}_m(E) = \frac{\bar{\zeta} D_0}{\bar{\zeta}_{\mathrm{thr}}} \left(\frac{E - E_{\min}}{E_{\max} - E_{\min}} \right)^2 \left[1 - \frac{1}{1 + e^{(E_{\mathrm{m}} - E_{\mathrm{aver}})/E_0}} \right] \quad (3),$$

where $E_{\min}$ and $E_{\max}$ are the minimum and maximum substrate stiffness locally sensed by the cell.

$\bar{\zeta}_{\text{thr}}$ is the thresholds of cell contractility and cooperates with the substrate stiffness to characterize the sensitivity of cells to the substrate stiffness gradient. $E_{\text{aver}} = \langle E \rangle_{c \geq c_0/2}$ is the average substrate stiffness sensed by the cell. E_{m} and E_0 are the threshold of stiffness sensitivity and the reference substrate stiffness, respectively, which regulate the most sensitive range of stiffness for cells. With density of actin and NMIIA defined above, the global polarity vector of cell is determined by the unit vector $\bar{\mathbf{n}}_{\text{polar}}$ of $\mathbf{n}_{\text{polar}} = \sum_{\mathbf{r}} \mathbf{r} / \sum_{\mathbf{r}} m - \langle \mathbf{r} \rangle_{c \geq c_0/2}$, which points from the center of NMIIA to the cell centeroid. As evidenced in our experiment, the local polarity of actin flow $\mathbf{P}$ is aligned to $\bar{\mathbf{n}}_{\text{polar}}$ (Movie 6-10). Therefore, the evolution of actin polarity field can be formulated by (43, 44):

$$\frac{\partial \mathbf{P}}{\partial t} + \left[\left(\mathbf{v} + w\mathbf{P} \right) \cdot \nabla \right] \mathbf{P} = -\underline{\underline{\Omega}} \cdot \mathbf{P} + \xi \underline{\underline{v}} \cdot \mathbf{P} - \frac{1}{\Gamma} \frac{\delta F}{\delta \mathbf{P}} - \bar{\zeta} \left[\mathbf{P} \cdot \left(\mathbf{n}_{\text{polar}} \mathbf{R}_{\pi/2} \right) \right] \mathbf{P} \mathbf{R}_{\pi/2} \quad (4),$$

where $\underline{\underline{\Omega}}$ and $\underline{\underline{v}}$ are the anti-symmetric and asymmetric part of $\nabla \mathbf{v}$, respectively; Γ denotes the rotational viscosity and $\mathbf{R}_{\pi/2}$ is a rotational matrix.

The proposed model successfully recapitulates amoeboid durotaxis found in our experiments, as shown in Fig. 5C-E. Initially, actin polarity $\mathbf{P}$ is assumed to be random (Fig. 5C). With increasing time, $\mathbf{P}$ tends to align along the stiffness gradient (Fig. 5D, Movie 16). In addition, asymmetric distribution of NMIIA is observed in our simulation, where NMIIA displays high concentration at the rear of the cell (Fig. 5E), consistent with our experiments (Fig. 3F).

Result 6 Cell contractility and substrate stiffness concertedly regulate amoeboid durotaxis

Our experiments show that decreasing cell contractility can inhibit amoeboid durotaxis. We theoretically demonstrate that with low cell contractility $\bar{\zeta}$, amoeboid durotaxis disappears and random trajectories of cells are observed (Fig. 6A). With increasing $\bar{\zeta}$, cells indeed perform directional migration along the stiffness gradient (Fig. 6B). To quantify amoeboid durotaxis in our model, we also calculate the FMI (Fig. 6E), similar to experimental statistics. Increased FMI indicates stronger amoeboid durotaxis. It is evident that with increasing cell contractility $\bar{\zeta}$, FMI elevates, accompanied by more robust amoeboid durotaxis.

Our model suggests that basal diffusion rate of NMIIA is larger on softer substrate, improving the mechanosensity of cells to substrate gradient, which is indirectly confirmed by previous experiments that NMIIA was more diffusive on softer substrates (6). In addition, the

model predicts that cells initially placed on softer region of gradient substrates exhibit stronger durotaxis (Fig. 6C-E). Furthermore, the initial local substrate stiffness may reverse cell durotaxis to adurotaxis. For example, under cell contractility $\bar{\zeta}=0.002$, cells on softer region of gradient substrate, i.e., initial stiffness of cell centroid E=30 and 70 kPa, migrate directionally following the stiffness gradient, whereas the strong durotaxis gives way to random migration when the initial stiffness of cell centroid is 200 kPa (Fig. 6D), resulting in an FMI close to zero (Fig. 6E). To verify our theoretical predictions, we segregate the gradient gel (ranging from 30 kPa to 210 kPa) into three equal regions (soft, medium and stiff) (Fig. 6F) for cell trajectory analysis. FMI of cells on the soft region ranked highest, while cells in the stiff region display more random motility (Fig. 5G). Cell velocity and persistence show no difference among these regions (Fig. 6H, I). These experiments faithfully agree with our theoretical predictions, thereby confirming the robustness regulation of amoeboid durotaxis by the local stiffness region.

Discussion

Durotaxis based on focal adhesion dependent mechanosensing has been well studied for decades. However, the concept that whether cell can durotax using amoeboid migration strategies was proposed only very recently (5). In this study, we developed an imaging-based cell migration device that provided both spatial confinement and stiffness gradient, and with this device we concluded that amoeboid cells can durotax. We further uncovered the underlying mechanism to involve NMIIA polarization towards the soft-matrix-side but may not require differential actin flow up- or down-stiffness gradient.

An intriguing question remains is how cells manage to retain NMIIA on regions that downward the stiffness gradient. One likely explanation would be that NMIIA could sense substrate stiffness (6) and then locates itself in the soft end. In our modeling, we assigned NMIIA with an initial diffusion rate which increases with higher substrate stiffness. Under this consideration, NMIIA is more diffusive on the stiff end and intended to accumulate on the soft end. To experimentally verify this, future work using single particle tracking is required to analyze NMIIA diffusion rate on substrate with different stiffness. Another possible mechanism may be that NMIIA is recruited by its upstream factors which prefer to locate at softer area. Mst1 kinase is a key component of Hippo pathway that could be regulated by substrate stiffness. It has been reported that Mst1 directly regulate NMIIA dynamics to organize high and low affinity LFA-1 to the anterior and posterior membrane during T cell migration (45). Whether Mst1 is mechanosensitive and has the capacity to recruit NMIIA to the soft end still need to be testified.

Aside from NMIIA, other mechanisms may also facilitate amoeboid durotaxis. The Arp2/3-branched actin has been implicated in stiffness induced migration of several cancer cell lines (7). However, when we treated T cells and neutrophils with the Arp2/3 inhibitor CK-666, no obvious changes in durotactic FMI, cell velocity or persistence were observed. CK-666 completely prohibited *Dictyostelium* motility at the concentration of 100 μM (not shown), hampering our further testing. Currently, these results do not support Arp2/3-branched actin being essential in amoeboid durotaxis.

The classical molecular clutch motor for mesenchymal durotaxis has concluded that the actin flow is mechanosensitive (30) – with low speed on stiff substrate and high speed on soft matrix. In our study, we also identified that actin flow speed can respond to substrate stiffness in a certain range (Fig. 2A). However, the actin flow did not show different velocity in up- or down- gradient part of a cell (Fig. 2B). These results indicate that the molecular clutches may also exist in amoeboid cells, but may not be sufficient to induce obvious actin flow difference within the single cell scale. Whether sharpening the stiffness gradient may produce differentiated actin flow in up- and down- gradient regions of a cell is yet to be tested. In that case, actin flow may add another layer of regulation on amoeboid durotaxis.

Inorganic droplets can move directionally on surfaces with stiffness gradient due to the intrinsic wettability (46). Droplets with smaller and wetting contact angles move towards the soft end, while those with larger and non-wetting contact angles can durotax (46). We also measured the contact angles of dHL-60 cells at both the stiffer and softer sides on gradient gel and observed non-wetting contact angles (greater than 90 degrees) on both sides albeit the angles on the softer side are larger. Hence, it can be postulated that the smaller, non-wetting contact angle on stiffer side are also likely contribute to amoeboid durotaxis to certain extent.

Immune cell activation is regulated not only by biochemical factors, but also by the mechano-microenvironment including substrate stiffness (47). Substrate rigidity influences differentiation (48), gene expression, cell migration, morphology, and cytokine secretion (22) in T cells. It has been established that tumor cell stiffness is negatively correlated with metastatic potential (49). Interestingly, cytotoxic T lymphocytes (CTL) has been shown to enhance killing response when encountering stiffer target cells (50). Whether stiff tumor cells can act as a mechanical guidance for CTL durotaxis is tentative to test. Immune cells are recruited and play a crucial role in tissue repair. Tissue injuries of varying origins, including chemical, mechanical, or microbiological, initiate the processes that ultimately result in fibrosis (51). Fibrosis is characterized by tissue stiffening due to excessive extracellular matrix protein deposition and cross-linking (3). It will be intriguing to investigate whether the rigidity cues in fibrotic area may regulate immune cell

migration.

The search for molecular mechanisms underlying cell durotaxis has been paralleled by the development of different types of theoretical models (30). The well-established motor-clutch model (52) and random walk model (53) demonstrate that cell durotaxis is attributable to traction or cell-substrate adhesion difference. These models, which usually ignore the asymmetric distribution of polarity markers, are more suitable for mesenchymal cells forming obvious stress fibers, but might not be applicative in low adhesive amoeboid cells. In contrast, polarized NMIIA contributes to durotaxis of amoeboid cells. The mechanosensing active gel model established here highlights the role of polarity markers in migration of cells with low adhesion. It also provides us a novel perspective that the diffusion rate difference dependent on substrate stiffness can polarize NMIIA and subsequently induce polarized actin flow along the stiffness gradient, followed by amoeboid durotaxis.

Materials and Methods

Cell lines and cell culture

The HL-60 cell line (derived from a 36-year-old female with acute promyelocytic leukemia) was purchased form National Infrastructure of Cell Line Resource (NICR). Human embryonic kidney 293T (HEK 293T) cells were kept by our laboratory. All cells were passed no more than 10 times and were mycoplasma free. HL-60 cells were cultured in RPMI-1640 medium (Hyclone, SH30809.01) supplemented with 15% fetal bovine serum (FBS; Vistech, VIS00CU3524), 100 U/mL penicillin and 100 μg/mL streptomycin at 37□ with 5% CO_2. The cultured cells were diluted once every 2-3 days into a density of $1*10^6$ cells/mL. For differentiation, HL-60 cells were diluted into RPMI-1640 medium containing 1.3% DMSO (VWR Life Science) with an initial density of $1*10^6$ cell/mL. For all the experiments, only cells differentiated for 5-6 days were used. HEK 293T cells were cultured in Dulbecco's modified Eagle medium (DMEM; Corning, 10-013-CRVC) supplemented with 10% FBS, 100 U/mL penicillin and 100 μg/mL streptomycin at 37□ with 5% CO_2. For cell passage, cells were washed with phosphate-buffered saline (PBS; Macgene, CC010) and digested with 0.25% trypsin (Macgene, CC012).

Dictyostelium cells were maintained in HL5 medium containing G418 (10-40 μg/ml), Hygromycin (50 μg/ml), or both as needed, as described in (54).

Gradient or uniform polyacrylamide (PA) gel preparation and functionalization

PA gel preparation and functionalization have been adapted from the previous work in our laboratory (26, 27). Specially, 40% acrylamide and 2% bis-acrylamide solutions were combined

at 11.73% and 0.33%, respectively, to make a 55kPa gel. 0.5% (w/v) Irgacure 2959 was added to catalyze cross-linking when exposed to UV light. Gels were cast on glutaraldehyde□modified cover glasses which was treated with bind-silane (BioDee, Beijing, China) followed by treatment with 0.5% glutaraldehyde (Sangon Biotech, Beijing, China) solution. To ensure complete polymerization, the whole acrylamide mix solution was first exposed to the UV light for 10 min without covering (for the initial nucleation in the polymerization reaction). To make gradient stiffness, an opaque mask was put between the gels and UV light. Then the mask was removed slowly by a microinjection pump with constant speed (40 μm/s for 10 min) to produce the steep stiffness gradient gels. After polymerization, the upper coverslip was peeled off the gel, leaving a thin layer of gel on the activated surface. The PA gel was then washed extensively in PBS. The PA gel was functionalized with 2 mL soak solution (137 mM NaCl and 5% (v/v) glycerol) for 1 h at room temperature. After that, 2 mL mixed buffer (pH 4.5) containing 15mM 1-ethyl-3-[3-dimethylaminopropyl] carbodiimide hydrochloride (EDC), 25mM N-hydroxysulfosuccinimide (NHS), 100mM 2-(N-morpholino) ethane sulfonic acid (MES) and 10% (v/v) glycerol were added. The PA gel was incubated within the mixed buffer in dark at room temperature for 30 min. Then, the PA gel was coated with fibronectin (50 μg/mL) or ICAM-1 (10 μg/mL) diluted in PBS for 35 min at room temperature. The PA gel was then washed with PBS three times and stored at 4□ for up to 1 week. The stiffness was measured with atomic force microscopy (AFM).

Uniform PA gels were made from 40% acrylamide and 2% bis-acrylamide mixed with 10% ammonium persulfate and 1% TEMED, where varying ratios of acrylamide and bis-acrylamide were used to create gels of known reproducible stiffness (55). The stiffness was measured with AFM.

2D confinement assay

Cells were seeded on the functionalized gradient gel or uniform gel and settled down for about 30 min. The culture medium was aspired and a small amount of medium was left on the glass bottom to prevent detachment and desiccation of the cells. The 0.5% agarose (SeaKem GTG Agarose, LONAZ) was diluted in RPMI-1640 medium without serum. The agarose was melted in the microwave oven and avoid superheating. The agarose solution was sandwiched between two pieces of cover slides and allowed hardening for about 5 min After hardening, the trimmed agarose gel was carefully placed on top of the cells adhered to the PA gel using the scalpel. The confinement device was incubated at 37□ for at least 30 min allowing the cells to adapt to increased stress in the physical confinement before imaging. Unless otherwise stated, all durotaxis assay were proceeded with this confinement device.

Mice

Male C57BL/6 WT mice were obtained from a special pathogen-free facility at Peking University Care Industrial Park, and were used for experiments at the age of 4-6 weeks. All procedures were approved and monitored by the Animal Care and Use Committee of Peking University.

Isolation of murine neutrophils

Bone marrow-derived neutrophils were isolated by Percoll gradients as described by Yunqiao Li et al (56). Mice were euthanized and bone marrow was extracted from the femurs by perfusing 6 mL pre-cold FACS solution (PBS with 2% FBS). Bone marrow cells were pelleted by centrifugation (300 g, 5 min, 4□) and then resuspended in 2 mL FACS. Percoll solution (Pharmacia) and 10× PBS were mixed (Percoll: 10× PBS = 9:1) to obtain a 100% Percoll stock. 100% Percoll stock was diluted with 1× PBS to get 72%, 60%, and 52% Percoll solutions. Bone marrow cell suspensions were loaded in the uppermost layer. After centrifugation (1100 g, 30 min, 4□), the neutrophils were collected in the band between the 72% and 60% layers. Before experiment, the neutrophils were stimulated with 100 nM fMLP (N-formyl-methionyl-leucyl-phenylalanine) (Sigma, F3506) for 10 min.

$CD4^+$ Naïve T cell purification

Mice were euthanized and the spleens were harvested and homogenized with a 40-μm cell strainer. After removing red blood cells by ACK (Ammonium-Chloride-Potassium) lysis, untouched primary naïve T cells were isolated with an EasySep Mouse T cell Isolation Kit according to the manufacturer's protocol (BioLegend). The purified $CD4^+$ Naïve T cells were stimulated with 20 ng/mL phorbol 12-myristate13-acetate (PMA) and 1 μg/mL ionomycin for 4-6 h to activate the integrin pathway before migration assay. Interaction between Lymphocyte Function-Associated Antigen 1 (LFA-1) and its ligand Intercellular Adhesion Molecule 1 (ICAM-1) has been reported to drive T cell movement by creating tangential friction between the actin cortex and the environment (23). In this case, T cells were allowed to migrate on the ICAM-1 coated surface.

Western blot

For Western blotting, suspended HL-60 cells were harvested and centrifuged at 300 g for 5 min and then washed with PBS once. Cells were lysed in radio immunoprecipitation assay (RIPA)

buffer (50 mM Tris-HCl pH 8.0, 150 mM NaCl, 1% Triton X-100, 0.5% Na-deoxycholate, 0.1% SDS, 1 mM EDTA, and protease inhibitor cocktail) for 10 min on ice. Lysates were centrifuged at 12,000 rpm for 10 min at 4 □, and the supernatants were collected. 5× SDS loading buffer was added to the supernatants and the mixture were boiled for 10 min at 95 °C. Protein samples were run on 10% SDS PAGE [H2O, 30% acrylamide, 1.5 M Tris-HCl pH 8.8, 10% ammonium persulphate, and tetramethylethylenediamine (TEMED)] and transferred onto nitrocellulose membranes by wet electrophoretic transfer, followed by 10% nonfat-milk blocking at room temperature for 1 h. The primary antibody incubations were at 4°C overnight or at room temperature for 2 h, followed by the secondary antibody incubations at room temperature for 1 h. The X-ray film was used to detect and record the band intensities. The fixed X-ray film was scanned, and digital images were obtained.

Immunofluorescence and imaging analysis

Cells were plated on acid-washed coverslips coated with 10 μg/mL fibronectin at room temperature for 30 min. Cells were then fixed with 4% paraformaldehyde at room temperature for 15 min, permeabilized with 0.5% Triton X-100 in PBS for 5 min, washed with PBS once for 5 min, and sequentially blocked with 10% bovine serum albumin (BSA) for 1 h at room temperature. Then, the primary antibody was appropriately diluted in PBS and cells were incubated for 1 h at room temperature. After washing with PBS three times, the cells were incubated with Alexa Fluor 488- or Alexa Fluor 555-conjugated secondary antibody (Thermo Fisher Scientific) for 1 h at room temperature. After washing in PBS three times, the coverslips were mounted with Prolong Diamond Antifade and DAPI (Thermo Fisher Scientific). After mounting medium is solidified, images were captured using Andor Dragonfly confocal imaging system.

Live cell imaging and durotaxis analysis

The activated T cells and neutrophils were plated on the PA gel which was previously coated ICAM-1 or fibronectin respectively. 30 min after seeding, PBS was used to wash out non-adhered cells and then fresh L-15 medium (Sigma, SLCG9244) with 20% FBS was added for imaging. Time-lapse videos were acquired for 15 min at 15 s intervals using a 10× dry objective lens (NA 0.3, Olympus, Tokyo, Japan) on a deconvolution microscope (CellTIRF). Images were analyzed with “manual tracking” and “chemotaxis tool” plugins of ImageJ. Coordinates and distances of cell movement were tracked using the ‘Manual Tracking’ plugin of ImageJ, then tracking data were imported into the ‘Chemotaxis Tool’ plugin to generate statistic feature such as velocity,

FMI (forward migration index), directionality and plot feature such as rose plot.

Antibodies and reagents

The following antibodies were used in this study: anti-GAPDH (ab181602) from Abcam; anti-MYH9 (A16923) and anti-MYH10 (A12029) from ABclonal; anti-Paxillin (AB_39952) from BD_Biosciences.

The following reagents were used in this study: Blebbistatin (2946047) from EMD_Millipore; Rho activator II (CN03) and SiR-Actin (CY-SC001) from Cytoskeleton; nocodazole (M1404) from Sigma-Aldrich.

Drug treatment

Drug treatment was performed according to previous publications. Blebbistatin was used at concentration of 10 μM and pre-treated for 10 min before imaging. Rho activator II was used at concentration of 0.25 μg/mL and pre-treated for 2 h before imaging. Nocodazole was used at concentration of 32 μM and pre-treated for 10 min before imaging (38). Taxol was used at concentration of 70 nM and pre-treated for 10 min before imaging (38). All drugs were incubated for the whole experiment.

Actin flow analysis

Quantitative fluorescence speckle microscopy (qFSM) was applied to analysis the actin flow of HL-60 cells on different PA gel. In general, HL-60 cells pretreated with 0.1 μM SiR Actin for 30 min were plated on PA gel as described above. Live cell movies were obtained for 2 min using a 63× 1.4 NA objective lens on Andor Dragonfly confocal imaging system. Movies were analyzed using a previously described quantitative Fluorescent Speckle Microscopy (qFSM) software in MATLAB (32). Full cell masks were generated using automatic thresholding (MinMax setting). Flow analyses were performed using the flow tracking setting with a six-frame integration window. The average actin flow rate was calculated for each movie (n = 10-20 cells per group). To compare the overall fluorescence of the cells used in QFSM, an ROI encompassing the cell perimeter was made and the mean fluorescence intensity of this ROI was recorded for each cell.

NMIIA and NMIIB knockdown cell line generation

The following short hairpin RNA (shRNA) primer were used to generate NMIIA and NMIIB knockdown HL-60.

Human shRNA forward shNMIIA, 5′- GCCAAGCTCAAGAACAAGCAT-3’.

Human shRNA forward shNMIIB, 5'-GCCAACATTGAAACATACCTT-3'.

The plasmid, together with other helper plasmid (pCMV-VSV-G and psPAX2), were transfected to HEK 293T cells at 60-80 % confluence. The virus-containing supernatant was harvested 48 h later, and concentrated 100 fold. $1*10^5$ HL 60 cells were infected with 100 Ml concentrated virus supernatant, centrifuging at 1000 g for 2 h. Polybrene (hexadimethrine bromide) was added at a final concentration of 10 μg/mL to increase infection efficiency. The infected cells were verified by Western blotting.

Atomic Force Microscope (AFM) measurement

A Bioscope Resolve atomic force microscope (AFM, NT-MDT) mounted on an Olympus IX73 inverted microscope was used to investigate the mechanical properties of polyacrylamide gels made from different formulations. The inverted microscope was used to visually position the AFM tip with respect to the specimen. Silicon nitride probes with a squared pyramid tip (DNP, nominal cantilever spring constant = 0.06 N/m, Bruker) were used in this study. After system stabilization, the thermal tune method was used to determine the exact spring constant before each experiment. The Hertz-Sneddon model for pyramid tips was used to extract Young's modulus of the sample. For each indentation, the following parameters were used: 1 nN set point, 4.0 μm Z range, and an extend speed of 2.0 μm/s. A two-tailed Student's *t* test with unequal variance was used for subsequent quantification and analysis.

Mechanosensing active gel model

We construct a mechanosensing active gel theory to model amoeboid durotaxis, where the cell is represented by an active droplet and cell migration is described by the spatial-temporal evolution of actin density $c(\mathbf{r},t)$ of the droplet. The evolution of actin density is formulated as (15):

$$\frac{\partial c}{\partial t}+\nabla\cdot\left[c\left(\mathbf{v}+w\mathbf{P}\right)-M\nabla\frac{\delta F}{\delta c}\right]=0 \quad (5),$$

where M is thermodynamic mobility parameter, $w\mathbf{P}$ denotes the polymerization of actin filament, and F, expressed by Eq. 1, is the free energy that constrains actins within the droplet. The incompressible Navier–Stokes equation is invoked to describe fluid velocity $\mathbf{v}$ (15, 57):

$$\nabla\cdot\mathbf{v}=0,$$
$$\rho\left(\frac{\partial}{\partial t}+\mathbf{v}\cdot\nabla\right)\mathbf{v}=-\nabla P+\nabla\cdot\boldsymbol{\sigma}^{\text{total}}-\gamma\mathbf{v}, \quad (6)$$

where P is the isotropic pressure and γ is the friction coefficient. Total hydrodynamic stress $\boldsymbol{\sigma}^{\text{total}}$ includes four parts, including viscous stress $\boldsymbol{\sigma}^{\text{vis}}=\eta\left(\nabla\mathbf{v}+\mathbf{v}\nabla\right)$, elastic stress $\boldsymbol{\sigma}^{\text{ela}}$, interfacial stress between active and passive phase $\boldsymbol{\sigma}^{\text{int}}$, and active stress $\boldsymbol{\sigma}^{\text{act}}$ (58). η is the shear viscosity, and the elastic stress $\boldsymbol{\sigma}^{\text{ela}}$ is formulated as

$$\boldsymbol{\sigma}^{\text{ela}}=-\frac{1}{2}\left(\mathbf{P}\frac{\delta F}{\delta\mathbf{P}}-\frac{\delta F}{\delta\mathbf{P}}\mathbf{P}\right)+\frac{\xi}{2}\left(\mathbf{P}\frac{\delta F}{\delta\mathbf{P}}+\frac{\delta F}{\delta\mathbf{P}}\mathbf{P}\right)-\kappa\nabla\mathbf{P}\cdot\mathbf{P}\nabla \quad (7)$$

where ξ is a shape factor. We take $\xi=1.1$, which means shear-aligning rod-like actin are considered (59). The interfacial stress between the active and passive phase is calculated as

$$\boldsymbol{\sigma}^{\text{int}}=\left(f-c\frac{\delta F}{\delta c}\right)\mathbf{I}-\nabla c\frac{\partial f}{\partial\left(\nabla c\right)} \quad (8)$$

where $\mathbf{I}$ is the identity tensor and f denotes the free energy density, which has been given by the integrand in Eq. 1.

The integration is performed using a vorticity or stream-function finite difference scheme (60) on a square 128×128 domain with periodic boundary conditions, whose grid spacing is $\Delta x=\Delta y=1$. The initial circular droplet with radius $R=7\ \mu\text{m}$ is placed at the center of square domain. At the beginning, the unit polarity field $\mathbf{P}$ is randomly generated and the fluid velocity $\mathbf{v}$ is zero. A fourth-order Runge-Kutta method with time step $\Delta t=0.1$ is employed to implement the time integration. To normalize the system, three scales are chosen as: length scale $L=1\ \mu\text{m}$, time scale $T=10\ \text{ms}$ and force scale $F=100\ \text{nN}$. The parameters used in the simulations are chosen from previous work (15) and our experiments, which are provided in Table S1 in the supplementary material.

Statistical analysis

All the plots and statistical tests were performed using GraphPad Prism software. The presented values were displayed as mean ± SEM for at least three independent experiments (as indicated in the figure legends). The significance was calculated using unpaired, one-side/two-side Student's *t* tests on One-way ANOVA, as indicated. In all statistical teste, $P > 0.05$ was considered as not significant. *P* values were indicated in the figure legends.

Acknowledgments

We thank Prof. Dan Lv, Dr. Yuxing Huang, Dr. Yingxue Rong, Dr. Yuan Jin, Dr. Peng Shi,

Chunlei Zhang and Xiaoyu Ren from Peking University for technical support and data discussion. We thank Prof. Xiangdong Li from Chinese Academy of Sciences for sharing the NMIIA construct.

Funding:
National Natural Science Foundation of China grant 32122029 (CW)
National Natural Science Foundation of China grant 11922207 (BL)
National Key R&D Program of China grant 2017YFA0506500 (CW)
Clinical Medicine Plus X - Young Scholars Project, Peking University grant PKU2019LCXQ017 (CW, LS)
Clinical Medicine Plus X - Young Scholars Project, Peking University grant PKU2018LCXQ015 (CW, LS)

Author contributions:

Conceptualization: CW, XY
Methodology: CW, BL, XY, PC, YY
Investigation: XY
Visualization: XY, PC, CK, DL
Supervision: CW, BL, HC
Writing—original draft: XY, PC
Writing—review & editing: CW, BL, XY, PC, CK

Competing interests: no competing interests.

Figures and Tables

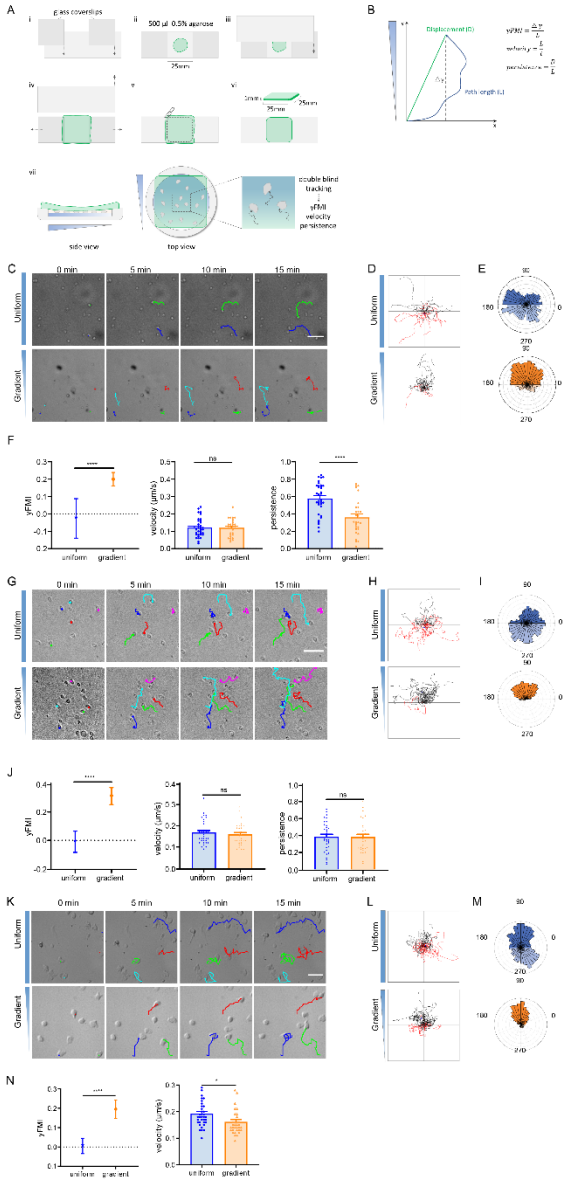

Fig 1. T cells and neutrophils undergo durotactic migration

(A) Illustration of 2D confinement assay combined with gradient PA gel.

(B) Illustration of FMI value calculation.

(C) Representative time-lapse images of single $CD4^+$ Naïve T cells migrating on ICAM-1 coated polyacrylamide gels with uniform stiffness (top, 30 kPa) and stiffness gradient (bottom, with greater stiffness towards the top, 20 kPa/mm). Color lines indicated the migration trajectories of single cell. Scare bar: 50 μm.

(D) Representative tracks of migrating $CD4^+$ Naïve T cells in Fig. 1A. n ≥ 30 tracks were analyzed for each experiment, N = 3 independent experiments for each condition, replicates are biological. Note that a higher proportion of cells migrate toward the stiffer end of the gradient substrate (black tracks) compared to cells migrating opposite to the gradient (red). Tracks on the uniform substrate showed equal proportion for each part.

(E) Angular displacement of $CD4^+$ Naïve T cells on the uniform stiffness gels (top) and stiffness gradient gels (bottom, with greater stiffness towards the top).

(F) y-FMI (Forward Migration Index), velocity and migration persistence for $CD4^+$ Naïve T cells cultured on uniform substrate or gradient substrate. All error bars are SEM ($n \geq 30$ tracks were analyzed for each experiment, N = 3 independent experiments for each condition, replicates are biological), ns, not significant, by Student's *t*-test.

(G) Representative time-lapse images of single neutrophils derived from mouse bone marrow migrating on ICAM-1 coated polyacrylamide gels with uniform stiffness (top) and stiffness gradient (bottom). Color lines indicated the migration trajectories of single cell. Scare bar: 50 μm.

(H) Representative tracks of migrating neutrophils in Fig. 1E. $n \geq 30$ tracks were analyzed for each experiment, n = 3 independent experiments for each condition, replicates are biological.

(I) Angular displacement of neutrophils on the uniform stiffness gels (top) and stiffness gradient gels (bottom, with greater stiffness towards the top).

(J) y-FMI, velocities and migration persistence for neutrophils cultured on uniform substrate or gradient substrate. All error bars are ± SEM ($n \geq 30$ tracks were analyzed for each experiment, N = 3 independent experiments for each condition, replicates are biological). ***, $P \leq 0.0005$, *, $P \leq 0.05$, by Student's *t*-test.

(K) Representative time-lapse images of differentiated HL-60 (dHL-60) cells on fibronectin coated polyacrylamide gels with uniform stiffness (top) and stiffness gradient (bottom). Color lines indicated the migration trajectories of single cell. Scare bar: 50 μm.

(L) Representative tracks of migrating dHL-60 cells in Fig. 2B. $n \geq 30$ tracks were analyzed for each experiment, n = 3 independent experiments for each condition, replicates are biological.

(M) Angular displacement of dHL-60 cells on the uniform stiffness gels (top) and stiffness gradient gels (bottom, with greater stiffness towards the top).

(N) y-FMI and velocities for dHL-60 cells cultured on uniform substrate or gradient substrate ($n \geq 30$ tracks were analyzed for each experiment, N = 3 independent experiments for each condition, replicates are biological). All error bars are SEM, ns, not significant, by Student's *t*-test.

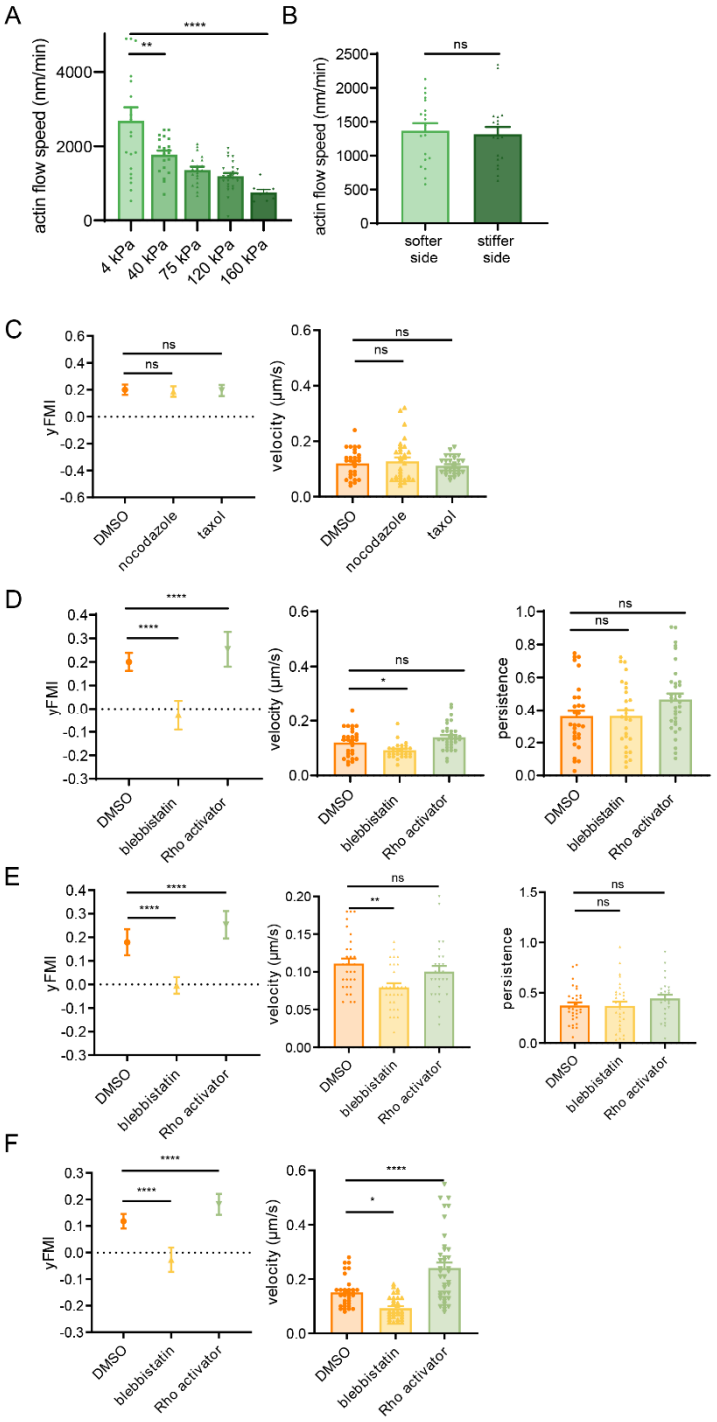

Fig 2. Amoeboid durotaxis may not be propelled by differential actin flow

(A) Actin flow speed of dHL-60 cells adhered on different substrate stiffness (4 kPa, 40 kPa, 75 kPa, 120 kPa and 160 kPa). Each plot indicated the average actin flow speed of every individual cell adhered on polyacrylamide gel. All error bars are SEM. **, $P \leq 0.005$, ****, $P < 0.0001$ by One-way ANOVA.

(B) Actin flow speed of softer side and stiffer side of the dHL-60 cells adhered on gradient substrate. Each plot indicated the average actin flow speed of every half part of individual

cells adhered on polyacrylamide gel. All error bars are SEM. ns, not significant, by Student's *t*-test.

(C) y-FMI and velocities of control (DMSO), nocodazole (32 μM, pre-treated for 10 min) treated and taxol (70 nM, pre-treated for 10 min) treated $CD4^+$ Naïve T cells moving on stiffness gradient gel (n ≥ 30 tracks were analyzed for each experiment, N = 3 independent experiments for each condition, replicates are biological). All error bars are SEM. ns, not significant, by One-way ANOVA.

(D) y-FMI, velocities and migration persistence of control (DMSO), blebbistatin (10 μM, pre-treated for 10 min) treated and Rho activator II (0.25 μg/ml, pre-treated for 2 h) treated $CD4^+$ Naïve T cells moving on stiffness gradient gel (n ≥ 30 tracks were analyzed for each experiment, N = 3 independent experiments for each condition, replicates are biological). All error bars are SEM. ****, $P < 0.0001$, *, $P \leq 0.05$, ns, not significant, by One-way ANOVA. All drugs were incubated for the whole experiment.

(E) y-FMI, velocities and migration persistence of control (DMSO), blebbistatin (10 μM, pre-treated for 10 min) treated and Rho activator II (0.25 μg/ml, pre-treated for 2 h) treated neutrophils moving on stiffness gradient gel (n ≥ 30 tracks were analyzed for each experiment, N = 3 independent experiments for each condition, replicates are biological). All error bars are SEM. ****, $P < 0.0001$, **, $P \leq 0.005$, ns, not significant, by One-way ANOVA. All drugs were incubated for the whole experiment.

(F) y-FMI and velocities of control (DMSO), blebbistatin (10 μM, pre-treated for 10 min) treated and Rho activator II (0.25 μg/ml, pre-treated for 2 h) treated dHL-60 cells moving on stiffness gradient gel (n ≥ 30 tracks were analyzed for each experiment, N = 3 independent experiments for each condition, replicates are biological). All error bars are SEM. ****, $P < 0.0001$, ns, not significant by One-way ANOVA.

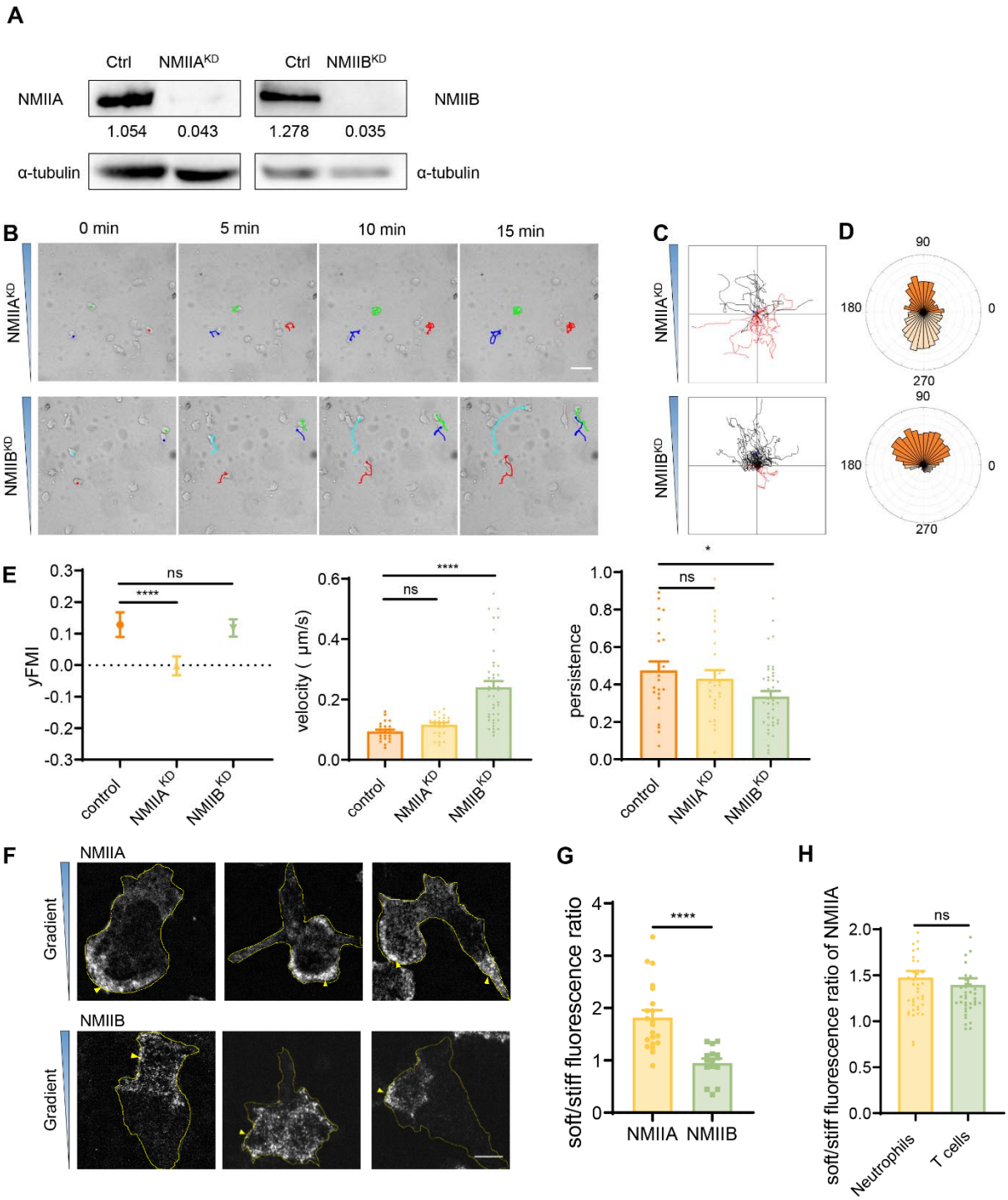

Fig 3. Durotaxis of T cells and neutrophils is regulated by polarized actomyosin activity

(A) Western blot showing the protein level of NMIIA (left) and NMIIB (right) in negative control (Ctrl), NMIIA knocked down (NMIIA^{KD}) and NMIIB knocked down (NMIIB^{KD}) HL-60 cells. α-tubulin was used as loading control. Numbers below the ladders were the relative intensity versus α-tubulin.

(B) Representative time-lapse images of NMIIA^{KD} (top) and NMIIB^{KD} (bottom) dHL-60 cells on

polyacrylamide gels with stiffness gradient. Color lines indicated the migration trajectories of single cell. Scare bar: 50 μm

(C) Representative tracks of migrating dHL-60 cells in Fig. 4D. n ≥ 30 tracks were analyzed for each experiment, n = 3 independent experiments for each condition, replicates are biological.

(D) Angular displacement of $NMIIA^{KD}$ (top) and $NMIIB^{KD}$ (bottom) dHL-60 cells on stiffness gradient gels (with greater stiffness towards the top).

(E) y-FMI, velocities and migration persistence of control, $NMIIA^{KD}$ and $NMIIB^{KD}$ dHL-60 cells moving on stiffness gradient gel (n = 32 for control, n = 30 for $NMIIA^{KD}$ and n = 48 for $NMIIB^{KD}$. n = 3 independent experiments for each condition, replicates are biological). All error bars are SEM. *, $P \leq 0.05$, ****, $P < 0.0001$, ns, not significant, by One-way ANOVA.

(F) Representative immunofluorescent staining of NMIIA (top) and NMIIB (bottom) of dHL-60 cells on stiffness gradient gel (with greater stiffness towards the top). The yellow triangles indicated the polarized location of NMIIA and NMIIB. Scale bar: 10 μm.

(G) Fluorescent intensity ratio of NMIIA or NMIIB in cell softer part to stiffer part in Fig. 4H. All error bars are SEM. ****, $P < 0.0001$, by Student's *t*-test.

(H) Fluorescent intensity ration of NMIIA in softer part to stiffer part of $CD4^+$ Naïve T cells and neutrophils in Fig. S3B, C. All error bars are SEM. ns, not significant, by Student's *t* test.

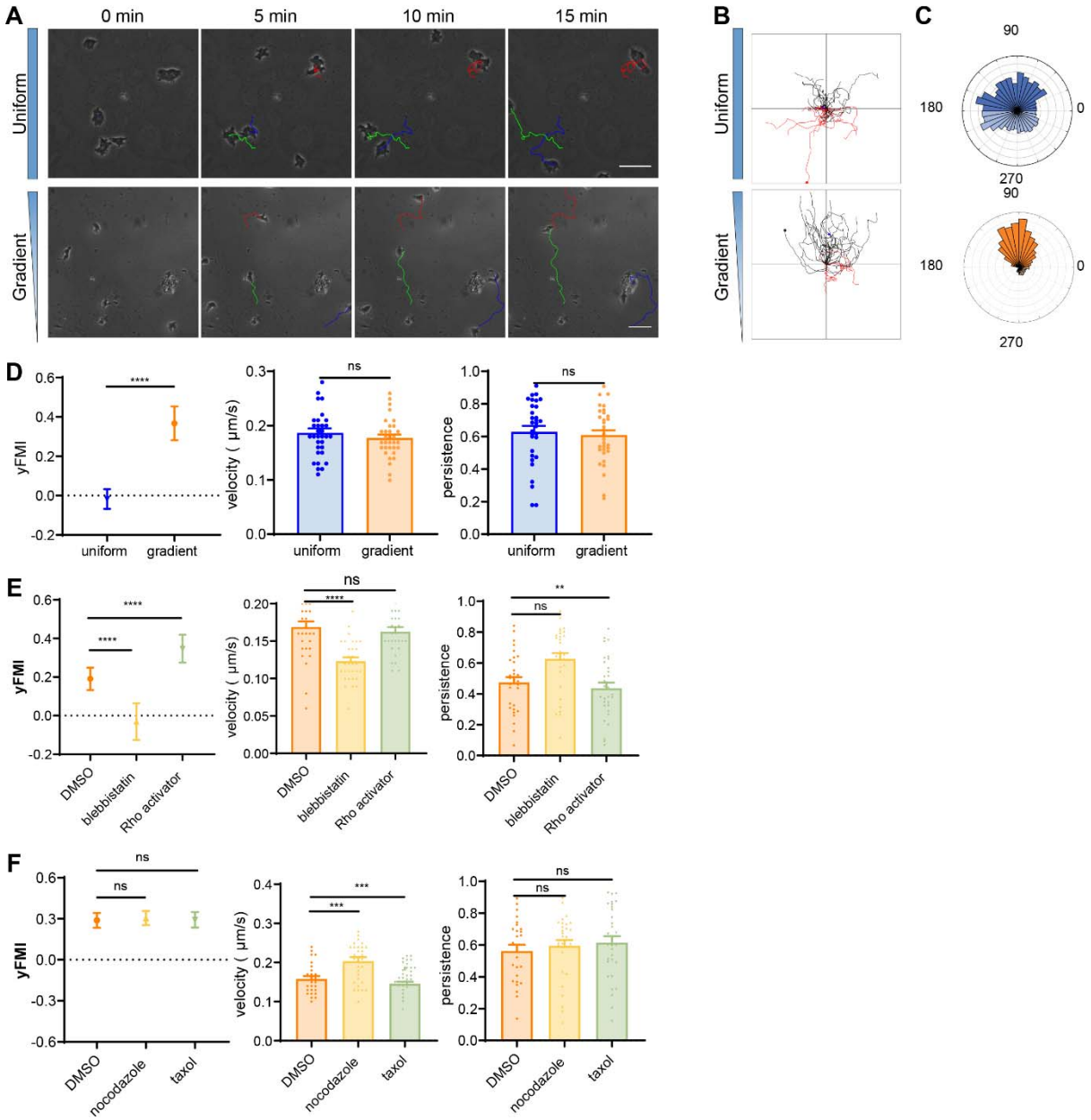

Fig 4. Amoeboid durotaxis is evolutionarily conserved

(A) Representative time-lapse phase contrast images of *Dictysotelium* on polyacrylamide gels with uniform stiffness (top) and stiffness gradient (bottom). Color lines indicated the migration trajectories of single cell. Scare bar: 50 μm.

(B) Representative tracks of migrating *Dictysotelium* in Fig. 3A. n ≥ 30 tracks were analyzed for each experiment, n = 3 independent experiments for each condition, replicates are biological.

(C) Angular displacement of *Dictysotelium* on the uniform stiffness gels (top) and stiffness gradient gels (bottom, with greater stiffness towards the top).

(D) y-FMI, velocities and migration persistence for *Dictysotelium* cultured on uniform substrate or gradient substrate. Error bars represent ± SEM (n ≥ 30 tracks were analyzed for each

experiment, N = 3 independent experiments for each condition, replicates are biological), ns, not significant, by Student's *t*-test.

(E) y-FMI, velocities and migration persistence of control (DMSO), blebbistatin (10 μM, pre-treated for 10 min) treated and Rho activator II (0.25 μg/ml, pre-treated for 2 h) treated *Dictysotelium* moving on stiffness gradient gel (n ≥ 30 tracks were analyzed for each experiment, N = 3 independent experiments for each condition, replicates are biological). All error bars are SEM. **, $P \leq 0.005$, ns, not significant, by One-way ANOVA.

(F) y-FMI, velocities and migration persistence of control (DMSO), nocodazole (32 μM, pre-treated for 10 min) treated and taxol (70 nM, pre-treated for 10 min) treated *Dictysotelium* moving on stiffness gradient gel (n ≥ 30 tracks were analyzed for each experiment, N = 3 independent experiments for each condition, replicates are biological). All error bars are SEM. ns, not significant, by One-way ANOVA.

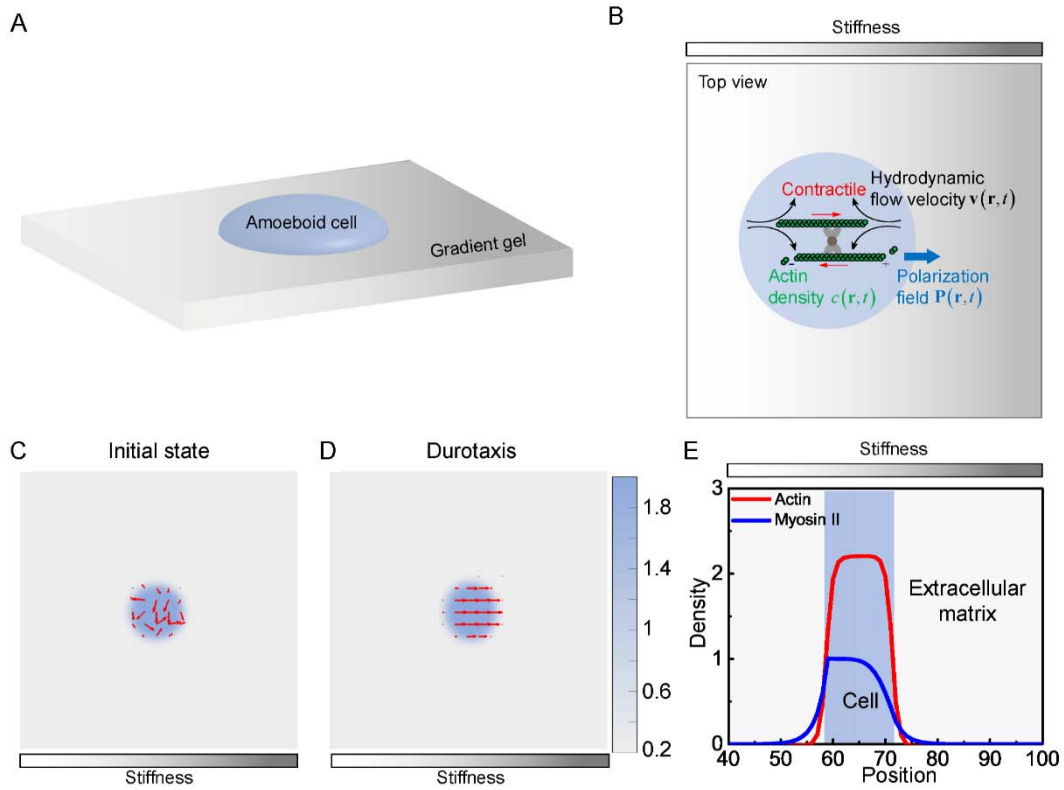

Fig 5. Mechanosensing active gel model of amoeboid durotaxis

(A) Illustration of an amoeboid cell crawling on the PA gel with stiffness gradient.

(B) Details of the mechanosensing active gel model. The blue circle represented an amoeboid cell. The position of the blue circle was defined by actin density (green) with given polarization field. To recapitulate cell migration, myosin contractility (red), and hydrodynamic flow

velocity (black) were illustrated in the model.

(C) Initial density and polarization field of actin. The background color indicated the density of myosin both inside and outside of the cell border. The red arrows indicated the polarization field of actin.

(D) Density and polarization field of actin during amoeboid durotaxis. The background color indicated the density of actin both inside and outside of the cell border. The red arrows indicated the polarization field of actin.

(E) Spatial distribution of NMIIA (blue line) and actin (red line) along the direction of stiffness gradient. The cell position was marked with the blue rectangle.

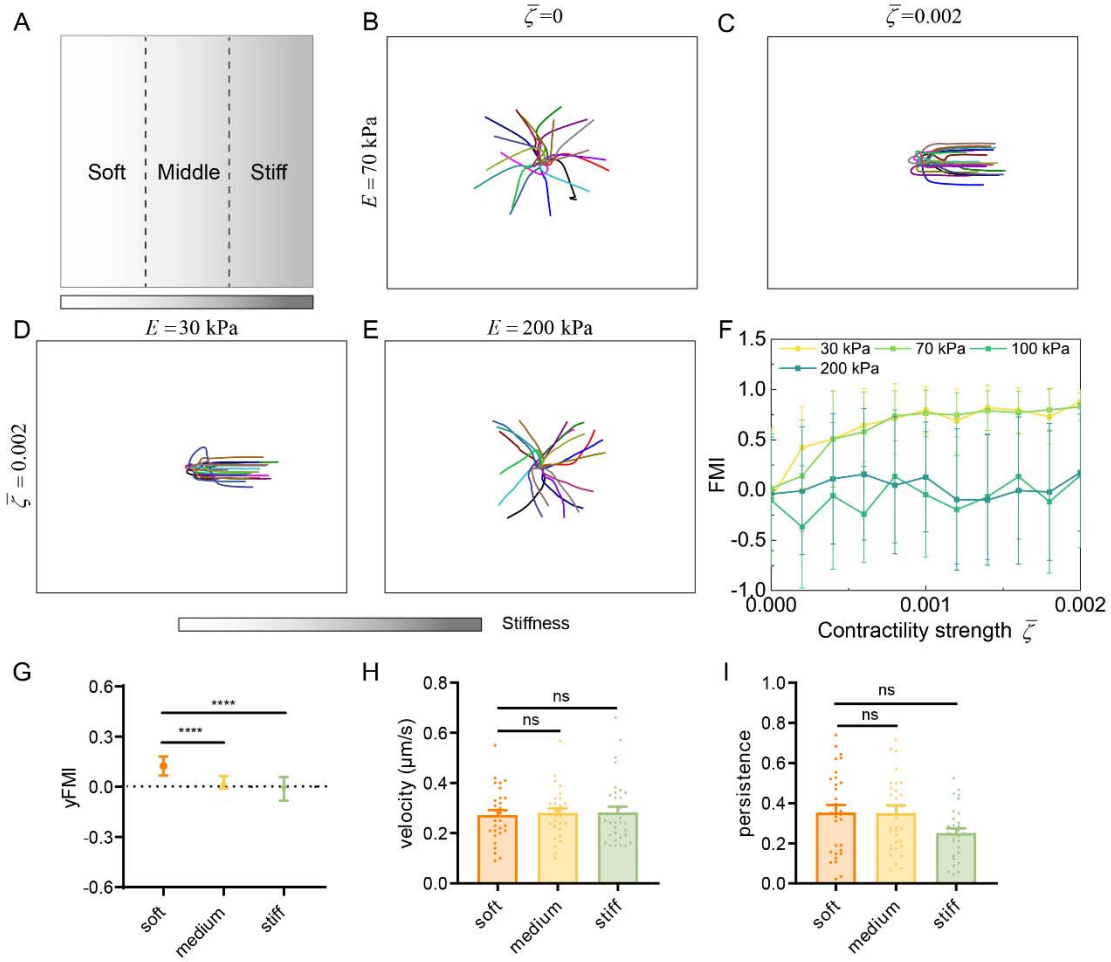

Fig 6. Regulation of amoeboid durotaxis by cell contractility and substrate stiffness

(A) Illustration of different regions (soft, medium and stiff) on gradient substrates with the greater stiffness towards right.

(B) Trajectories of migrating amoeboid cells with no contractility ($\bar{\zeta} = 0$) on medium region of gradient substrates, and the substrate stiffness of the initial cell centroid was set as E = 70 kPa.

(C) Trajectories of migrating amoeboid cells with normal contractility ($\bar{\zeta} = 0.002$) on medium region of gradient substrates, and the substrate stiffness of the initial cell centroid was set as E = 70 kPa.

(D) Trajectories of migrating amoeboid cells with normal contractility ($\bar{\zeta} = 0.002$) on soft region of gradient substrates, and the substrate stiffness of the initial cell centroid was set as E = 30 kPa.

(E) Trajectories of migrating amoeboid cells with normal contractility ($\bar{\zeta} = 0.002$) on stiff region of gradient substrates, and the substrate stiffness of the initial cell centroid was set as E = 200 kPa.

(F) The FMI with different contractility strength and different initial substrate stiffness of cell centroid.

(G-I) FMI, velocities and migration persistence of $CD4^+$ Naïve T cells migrating on different regions illustrated in Fig. 6A. $n \geq 30$ tracks were analyzed for each experiment, N = 3 independent experiments for each condition, replicates are biological. All error bars are SEM. ns, not significant, by One-way ANOVA.

Supplementary Materials

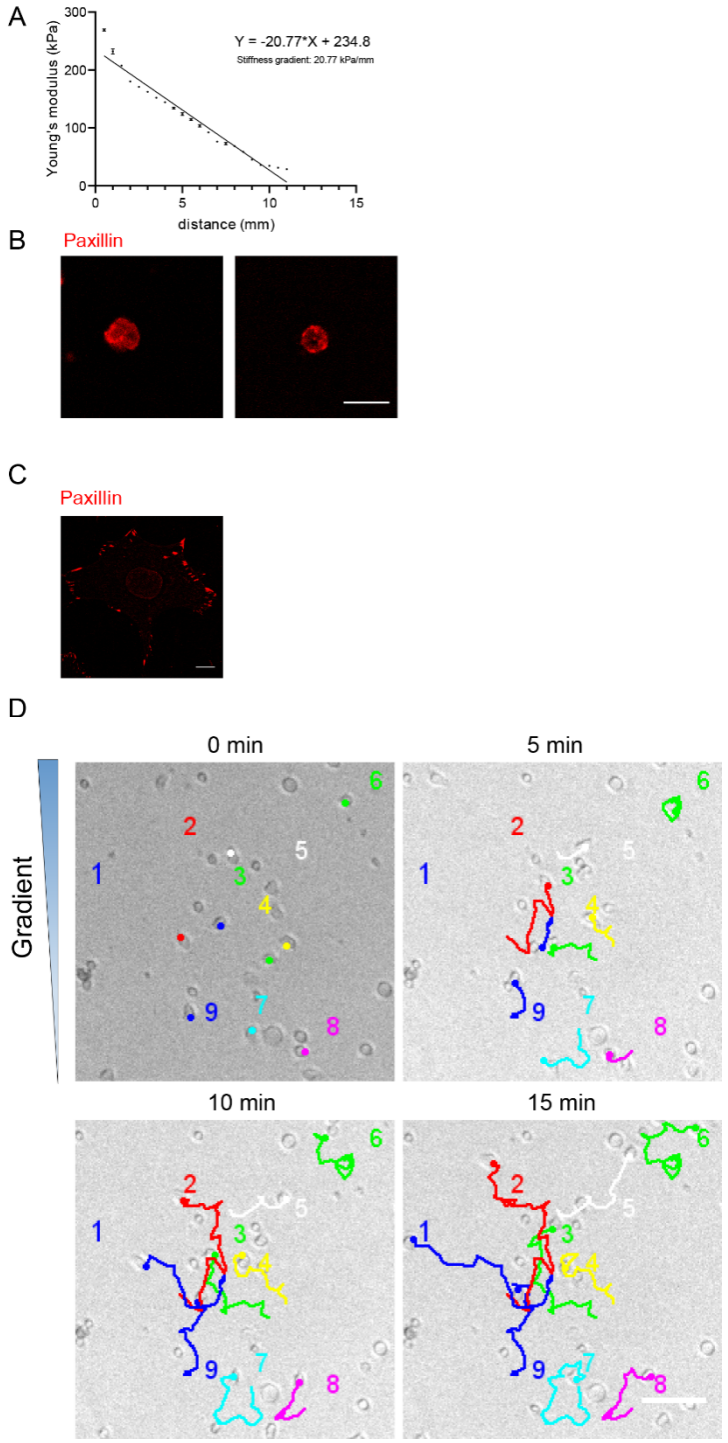

Fig S1.

(A) Representative stiffness gradient of polyacrylamide gels measured by atomic force microscope was plotted (20.77 kPa/mm). All error bars are SEM. (n = 3 regions, replicates are biological).

(B) Representative immunofluorescent staining of paxillin of $CD4^+$ naïve T cells on glass. Scale bar: 10 μm.

(C) Representative immunofluorescent staining of paxillin of MDA-MB 231 cells on glass. Scale

bar: 10 μm.

(D) Representative tracks of migrating neutrophils on stiffness gradient gel with greater stiffness towards the top. Color lines and numbers indicated the migration trajectories of single cell. Scare bar: 50 μm.

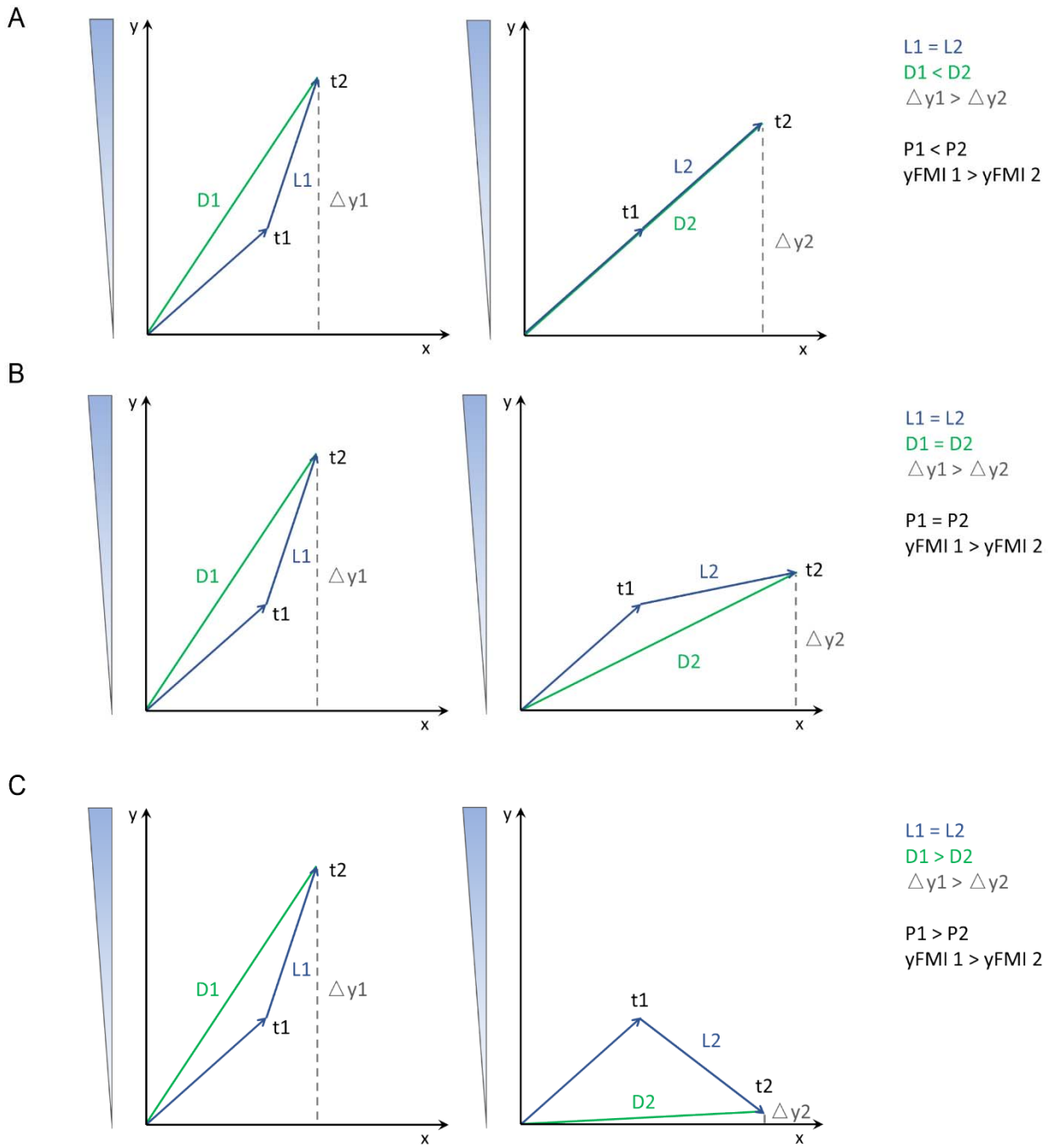

Fig. S2

Representative trajectories of three different conditions (A, B and C) of persistence value when the yFMI1 > yFMI2. In all conditions, the single cell migrated the same locomotion, which means L1 = L2. T1 and t2 can be regarded as the two consecutive time points during cell

migration. Each graph showed one condition for a migrating single cell. In all three conditions, yFMI on left was greater than the right. But the persistence on left was less, equal or greater than the right respectively.

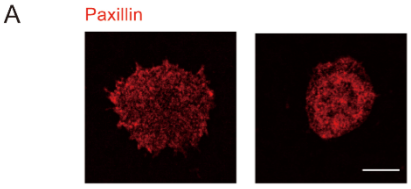

Fig S3.

(A) Representative immunofluorescent staining of paxillin of dHL-60 cells on glass. Scale bar: 10 μm.

.

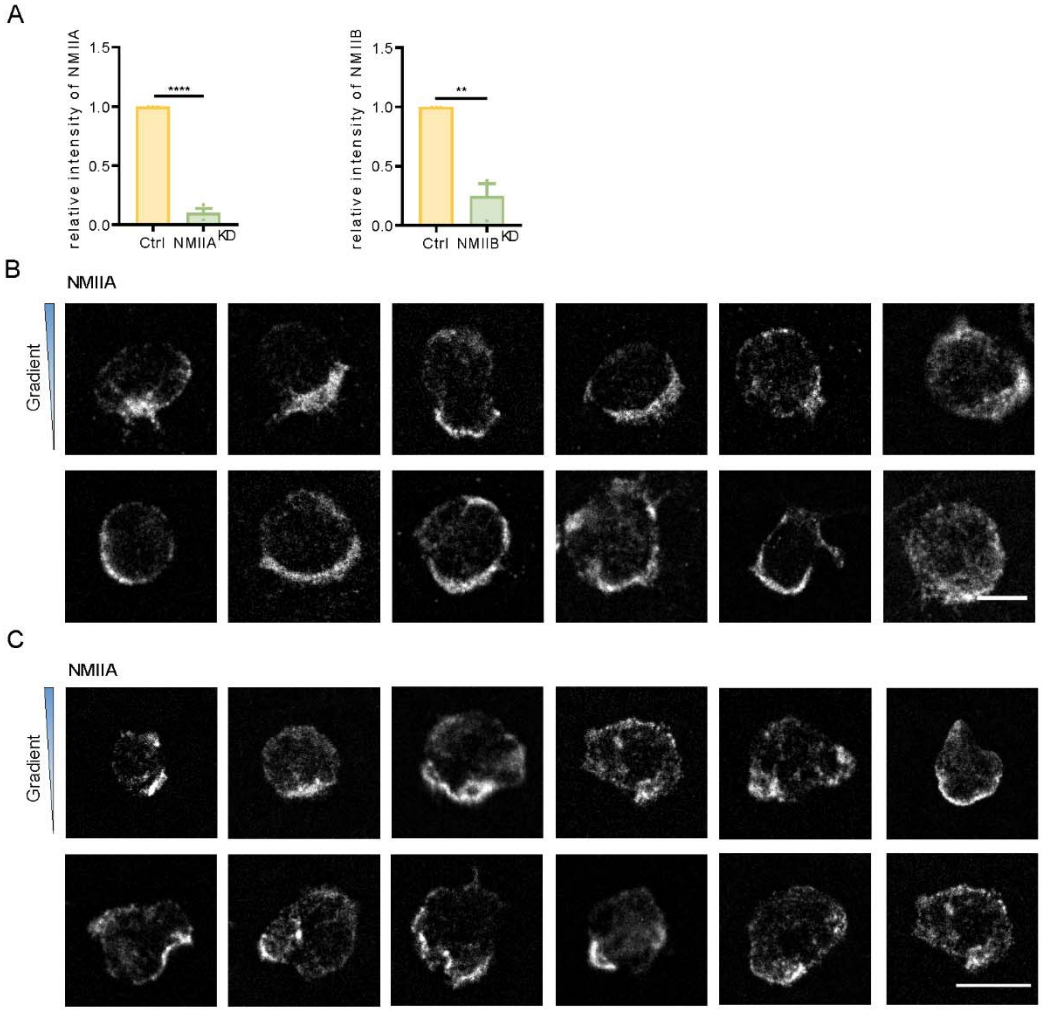

Fig S4

(A) Quantification of protein level in Fig. 4C. α-tubulin was used as loading control. Bar chart shows quantification of protein levels normalized to α-tubulin in each condition. All error bars are SEM. (n = 3 independent experiments, replicates are biological), ****, $P < 0.0001$; **, $P < 0.01$, by Student's *t*-test.

(B) Representative immunofluorescent staining of NMIIA of $CD4^+$ Naïve T cells on stiffness gradient gel (with greater stiffness towards the top). Scale bar: 5 μm.

(C) Representative immunofluorescent staining of NMIIA of neutrophils on stiffness gradient gel (with greater stiffness towards the top). Scale bar: 10 μm.

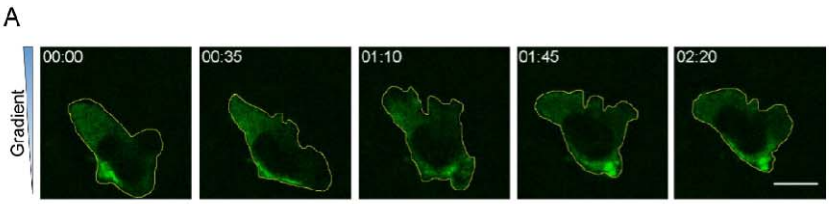

Fig S5

(A) Representative time-lapse images of GFP-NMIIA dHL-60 migrating on gradient gel with greater stiffness towards the top. Scale bar: 10 μm.

Table S1. Parameters used in simulations

Model parameters	symbol	Physical value	Simulation value
Effective shear viscosity	η	$1.67\ \mathrm{kPa\cdot s}$	5/3
Effective elastic constant	κ	$2\ \mathrm{nN}$	0.02
Interfacial tension	k	$10\ \mathrm{nN\cdot \mu m^6}$	0.1
Shape factor	ξ		1.1
Polymerization speed	w	$0.03\ \mu\mathrm{m/s}$	0.0003
Average density of actin	ς_0	$2\ \mu\mathrm{m}^{-3}$	2
Phenomenological amplitude	a	$10\ \mathrm{kPa}$	0.1
Mobility parameter	M	$0.1\ \mu\mathrm{m}^2/(\mathrm{kPa\cdot s})$	0.1
Rotational viscosity	Γ	$1\ \mathrm{kPa\cdot s}$	1
Stability constant	α	$10\ \mathrm{kPa}$	0.1
Fluid mass density	ρ	$10^{14}\ \mathrm{kg/m^3}$	10
Rotational viscosity of myosin	Γ_m	$5\ \mathrm{kPa\cdot s}$	5

Reference substrate stiffness	E_0	$1\,\mathrm{kPa}$	0.01
Stiffness gradient	E_g	$40\ \mathrm{kPa/mm}$	0.0004
Basal diffusion rate of NMIIA	D_0	$0.1\ \mu\mathrm{m}^2/\mathrm{s}$	0.1
Average concentration of NMIIA	m_0	$1\ \mu\mathrm{m}^{-3}$	1
Threshold of cell contractility	$\bar{\zeta}_{\mathrm{tr}}$	$0.1\ \mathrm{nN}\cdot\mu\mathrm{m}$	0.001

Movies:

Movie 1: Representative movie of fast crawling $CD4^+$ Naïve T cells on uniform gel in Fig. 1C. Color lines indicated the migration trajectories of single cell. Scare bar: 50 μm.

Movie 2: Representative movie of fast crawling $CD4^+$ Naïve T cells on gradient gel in Fig. 1C. Color lines indicated the migration trajectories of single cell. Scare bar: 50 μm.

Movie 3: Representative movie of fast crawling neutrophils on both uniform (first 59 frames) and gradient gel (last 60 frames) in Fig. 1G. Color lines indicated the migration trajectories of single cell. Scare bar: 50 μm.

Movie 4: Representative movie of fast crawling neutrophils on gradient gel in Fig. S1C. Color lines and numbers indicated the migration trajectories of single cell. Scare bar: 50 μm.

.

Movie 5: Representative movie of fast crawling dHL-60 cells on both uniform (first 59 frames) and gradient gel (last 59 frames) in Fig. 1K. Color lines indicated the migration trajectories of single cell. Scare bar: 50 μm.

Movie 6: Representative movie of dHL-60 cell stained with 0.1 μM SiR-Actin on 160 kPa substrate. Left: live cell movie of dHL-60 cell. Middle: raw movie of left panel integrated with actin flow vectors. Right: heat map of actin flow distribution for left panel. Scare bar: 10 μm.

Movie 7: Representative movie of dHL-60 cell stained with 0.1 μM SiR-Actin on 4 kPa substrate. Left: live cell movie of dHL-60 cell. Middle: raw movie of left panel integrated with actin flow vectors. Right: heat map of actin flow distribution for left panel. Scare bar: 10 μm.

Movie 8: Representative movie of dHL-60 cell stained with 0.1 μM SiR-Actin on 40 kPa substrate. Left: live cell movie of dHL-60 cells. Middle: raw movie of left panel integrated with actin flow vectors. Right: heat map of actin flow distribution for left panel. Scare bar: 10 μm.

Movie 9: Representative movie of dHL-60 cell stained with 0.1 μM SiR-Actin on 75 kPa substrate. Left: live cell movie of dHL-60 cells. Middle: raw movie of left panel integrated with actin flow vectors. Right: heat map of actin flow distribution for left panel. Scare bar: 10 μm.

Movie 10: Representative movie of dHL-60 cell stained with 0.1 μM SiR-Actin on 120 kPa substrate. Left: live cell movie of dHL-60 cell. Middle: raw movie of left panel integrated with actin flow vectors. Right: heat map of actin flow distribution for left panel. Scare bar: 10 μm.

Movie 11: Representative movie of both soft (first 40 frames) and stiff part (last 40 farmes) of dHL-60 cells stained with 0.1 μM SiR-Actin on gradient gel in Fig. 2B. Left: live cell movie of dHL-60 cells. Right: raw movie of left panel integrated with actin flow vectors. Scare bar: 10 μm.

Movie 12: Representative movie of fast crawling neutrophils on gradient gel with 10 μM blebbistatin treatment (first 60 frames) and 0.25 μg/ml Rho activator II treatment (last 60 frames) in Fig. 2E. Scare bar: 50 μm

Movie 13: Representative movie of both $NMIIA^{KD}$ (first 59 frames) and $NMIIB^{KD}$ dHL-60 cells (last 60 frames) migrating on gradient gel in Fig. 3B. Color lines indicated the migration trajectories of single cell. Scare bar: 50 μm.

Movie 14: Representative movie of a GFP-NMIIA dHL-60 cell migrating on gradient gel in Fig S5. Scare bar: 10 μm.

Movie 15: Representative movie of fast crawling *Dictyostelium* cells on both uniform (left) and gradient gel (right) in Fig. 4A. Color lines indicated the migration trajectories of single cell. Scare bar: 50 μm.

Movie 16: Representative movie of amoeboid durotaxis active gel model. The green arrows indicated the polarization field of actin. The background color indicated the density of myosin both inside and outside of the cell border. The white track indicated the migration trajectory of migrating amoeboid cell.

References

Uncategorized References

1. Trepat X, Chen Z, Jacobson K. Cell migration. Compr Physiol. 2012;2(4):2369-92.
2. Kindberg A, Hu JK, Bush JO. Forced to communicate: Integration of mechanical and biochemical signaling in morphogenesis. Curr Opin Cell Biol. 2020;66:59-68.
3. Wells RG. Tissue mechanics and fibrosis. Biochim Biophys Acta. 2013;1832(7):884-90.
4. Lo CM, Wang HB, Dembo M, Wang YL. Cell movement is guided by the rigidity of the substrate. Biophysical journal. 2000;79(1):144-52.
5. Espina JA, Marchant CL, Barriga EH. Durotaxis: the mechanical control of directed cell migration. FEBS J. 2022;289(10):2736-54.
6. Raab M, Swift J, P. Dingal PCD, Shah P, Shin J-W, Discher DE. Crawling from soft to

stiff matrix polarizes the cytoskeleton and phosphoregulates myosin-II heavy chain. The Journal of Cell Biology. 2012;199(4):669-83.
7. DuChez BJ, Doyle AD, Dimitriadis EK, Yamada KM. Durotaxis by Human Cancer Cells. Biophysical journal. 2019;116(4):670-83.
8. Sunyer R, Trepat X. Durotaxis. Curr Biol. 2020;30(9):R383-R7.
9. Shellard A, Mayor R. Durotaxis: The Hard Path from In Vitro to In Vivo. Dev Cell. 2021;56(2):227-39.
10. Sunyer R, Conte V, Escribano J, Elosegui-Artola A, Labernadie A, Valon L, et al. Collective cell durotaxis emerges from long-range intercellular force transmission. Science. 2016;353(6304):1157-61.
11. Plotnikov SV, Waterman CM. Guiding cell migration by tugging. Current opinion in cell biology. 2013;25(5):619-26.
12. Plotnikov SV, Pasapera AM, Sabass B, Waterman CM. Force fluctuations within focal adhesions mediate ECM-rigidity sensing to guide directed cell migration. Cell. 2012;151(7):1513-27.
13. Shannon MJ, Pineau J, Griffie J, Aaron J, Peel T, Williamson DJ, et al. Differential nanoscale organisation of LFA-1 modulates T-cell migration. J Cell Sci. 2019;133(5).
14. Hawkins RJ, Poincloux R, Benichou O, Piel M, Chavrier P, Voituriez R. Spontaneous contractility-mediated cortical flow generates cell migration in three-dimensional environments. Biophysical journal. 2011;101(5):1041-5.
15. Tjhung E, Marenduzzo D, Cates ME. Spontaneous symmetry breaking in active droplets provides a generic route to motility. Proc Natl Acad Sci U S A. 2012;109(31):12381-6.
16. Carles M, Pittet JF. Leukocyte chemotaxis and migration: can we follow the cells? Anesthesiology. 2010;113(3):512-3.
17. Stuelten CH, Parent CA, Montell DJ. Cell motility in cancer invasion and metastasis: insights from simple model organisms. Nat Rev Cancer. 2018;18(5):296-312.
18. Wu C, Asokan SB, Berginski ME, Haynes EM, Sharpless NE, Griffith JD, et al. Arp2/3 is critical for lamellipodia and response to extracellular matrix cues but is dispensable for chemotaxis. Cell. 2012;148(5):973-87.
19. Manahan CL, Iglesias PA, Long Y, Devreotes PN. Chemoattractant signaling in dictyostelium discoideum. Annual review of cell and developmental biology. 2004;20:223-53.
20. Stroka KM, Aranda-Espinoza H. Endothelial cell substrate stiffness influences neutrophil transmigration via myosin light chain kinase-dependent cell contraction. Blood. 2011;118(6):1632-40.
21. Schaefer A, Hordijk PL. Cell-stiffness-induced mechanosignaling - a key driver of leukocyte transendothelial migration. J Cell Sci. 2015;128(13):2221-30.
22. Saitakis M, Dogniaux S, Goudot C, Bufi N, Asnacios S, Maurin M, et al. Different TCR-induced T lymphocyte responses are potentiated by stiffness with variable sensitivity. Elife. 2017;6.
23. Hons M, Kopf A, Hauschild R, Leithner A, Gaertner F, Abe J, et al. Chemokines and integrins independently tune actin flow and substrate friction during intranodal migration of T cells. Nat Immunol. 2018;19(6):606-16.
24. Mihlan M, Glaser KM, Epple MW, Lammermann T. Neutrophils: Amoeboid Migration and Swarming Dynamics in Tissues. Front Cell Dev Biol. 2022;10:871789.
25. Litschko C, Damiano-Guercio J, Brühmann S, Faix J. Analysis of Random Migration of Dictyostelium Amoeba in Confined and Unconfined Environments. Methods in molecular biology (Clifton, NJ). 2018;1749:341-50.
26. Rong Y, Yang W, Hao H, Wang W, Lin S, Shi P, et al. The Golgi microtubules regulate single cell durotaxis. EMBO Rep. 2021;22(3):e51094.
27. Wang Y, Zhang C, Yang W, Shao S, Xu X, Sun Y, et al. LIMD1 phase separation

contributes to cellular mechanics and durotaxis by regulating focal adhesion dynamics in response to force. Dev Cell. 2021;56(9):1313-25 e7.
28. Bear JE, Haugh JM. Directed migration of mesenchymal cells: where signaling and the cytoskeleton meet. Curr Opin Cell Biol. 2014;30:74-82.
29. Collins SJ, Ruscetti FW, Gallagher RE, Gallo RC. Terminal differentiation of human promyelocytic leukemia cells induced by dimethyl sulfoxide and other polar compounds. Proc Natl Acad Sci U S A. 1978;75(5):2458-62.
30. Bangasser BL, Shamsan GA, Chan CE, Opoku KN, Tuzel E, Schlichtmann BW, et al. Shifting the optimal stiffness for cell migration. Nat Commun. 2017;8:15313.
31. Shin ME, He Y, Li D, Na S, Chowdhury F, Poh YC, et al. Spatiotemporal organization, regulation, and functions of tractions during neutrophil chemotaxis. Blood. 2010;116(17):3297-310.
32. Mendoza MC, Besson S, Danuser G. Quantitative fluorescent speckle microscopy (QFSM) to measure actin dynamics. Curr Protoc Cytom. 2012;Chapter 2:Unit2 18.
33. Gardel ML, Sabass B, Ji L, Danuser G, Schwarz US, Waterman CM. Traction stress in focal adhesions correlates biphasically with actin retrograde flow speed. The Journal of cell biology. 2008;183(6):999-1005.
34. Lim JI, Sabouri-Ghomi M, Machacek M, Waterman CM, Danuser G. Protrusion and actin assembly are coupled to the organization of lamellar contractile structures. Exp Cell Res. 2010;316(13):2027-41.
35. Jurado C, Haserick JR, Lee J. Slipping or gripping? Fluorescent speckle microscopy in fish keratocytes reveals two different mechanisms for generating a retrograde flow of actin. Mol Biol Cell. 2005;16(2):507-18.
36. Yolland L, Burki M, Marcotti S, Luchici A, Kenny FN, Davis JR, et al. Persistent and polarized global actin flow is essential for directionality during cell migration. Nat Cell Biol. 2019;21(11):1370-81.
37. Kopf A, Renkawitz J, Hauschild R, Girkontaite I, Tedford K, Merrin J, et al. Microtubules control cellular shape and coherence in amoeboid migrating cells. The Journal of cell biology. 2020;219(6).
38. Tabdanov ED, Rodriguez-Merced NJ, Cartagena-Rivera AX, Puram VV, Callaway MK, Ensminger EA, et al. Engineering T cells to enhance 3D migration through structurally and mechanically complex tumor microenvironments. Nat Commun. 2021;12(1):2815.
39. Callan-Jones AC, Voituriez R. Actin flows in cell migration: from locomotion and polarity to trajectories. Current opinion in cell biology. 2016;38:12-7.
40. Sandquist JC, Swenson KI, DeMali KA, Burridge K, Means AR. Rho kinase differentially regulates phosphorylation of nonmuscle myosin II isoforms A and B during cell rounding and migration. J Biol Chem. 2006;281(47):35873-83.
41. Jacobelli J, Chmura SA, Buxton DB, Davis MM, Krummel MF. A single class II myosin modulates T cell motility and stopping, but not synapse formation. Nat Immunol. 2004;5(5):531-8.
42. Van Haastert PJ. Amoeboid cells use protrusions for walking, gliding and swimming. PloS one. 2011;6(11):e27532.
43. Cates ME, Henrich O, Marenduzzo D, Stratford K. Lattice Boltzmann simulations of liquid crystalline fluids: active gels and blue phases. Soft Matter. 2009;5(20):3791-800.
44. Genkin MM, Sokolov A, Lavrentovich OD, Aranson IS. Topological Defects in a Living Nematic Ensnare Swimming Bacteria. Physical Review X. 2017;7(1):011029.
45. Xu X, Jaeger ER, Wang X, Lagler-Ferrez E, Batalov S, Mathis NL, et al. Mst1 directs Myosin IIa partitioning of low and higher affinity integrins during T cell migration. PloS one. 2014;9(8):e105561.
46. Bueno J, Bazilevs Y, Juanes R, Gomez H. Wettability control of droplet durotaxis. Soft Matter. 2018;14(8):1417-26.

47. Pageon SV, Govendir MA, Kempe D, Biro M. Mechanoimmunology: molecular-scale forces govern immune cell functions. Mol Biol Cell. 2018;29(16):1919-26.
48. O'Connor RS, Hao X, Shen K, Bashour K, Akimova T, Hancock WW, et al. Substrate rigidity regulates human T cell activation and proliferation. J Immunol. 2012;189(3):1330-9.
49. Swaminathan V, Mythreye K, O'Brien ET, Berchuck A, Blobe GC, Superfine R. Mechanical stiffness grades metastatic potential in patient tumor cells and in cancer cell lines. Cancer Res. 2011;71(15):5075-80.
50. Basu R, Whitlock BM, Husson J, Le Floc'h A, Jin W, Oyler-Yaniv A, et al. Cytotoxic T Cells Use Mechanical Force to Potentiate Target Cell Killing. Cell. 2016;165(1):100-10.
51. Tschumperlin DJ, Ligresti G, Hilscher MB, Shah VH. Mechanosensing and fibrosis. J Clin Invest. 2018;128(1):74-84.
52. Isomursu A, Park K-Y, Hou J, Cheng B, Shamsan G, Fuller B, et al. Negative durotaxis: cell movement toward softer environments. 2020:2020.10.27.357178.
53. Doering CR, Mao X, Sander LM. Random walker models for durotaxis. Phys Biol. 2018;15(6):066009.
54. Li D, Sun F, Yang Y, Tu H, Cai H. Gradients of PI(4,5)P2 and PI(3,5)P2 Jointly Participate in Shaping the Back State of Dictyostelium Cells. Front Cell Dev Biol. 2022;10:835185.
55. Fischer RS, Myers KA, Gardel ML, Waterman CM. Stiffness-controlled three-dimensional extracellular matrices for high-resolution imaging of cell behavior. Nat Protoc. 2012;7(11):2056-66.
56. Li Y, Jin Y, Liu B, Lu D, Zhu M, Jin Y, et al. PTENalpha promotes neutrophil chemotaxis through regulation of cell deformability. Blood. 2019;133(19):2079-89.
57. Tjhung E, Tiribocchi A, Marenduzzo D, Cates ME. A minimal physical model captures the shapes of crawling cells. Nat Commun. 2015;6:5420.
58. Hatwalne Y, Ramaswamy S, Rao M, Simha RA. Rheology of active-particle suspensions. Phys Rev Lett. 2004;92(11):118101.
59. Kung W, Marchetti MC, Saunders K. Hydrodynamics of polar liquid crystals. Phys Rev E Stat Nonlin Soft Matter Phys. 2006;73(3 Pt 1):031708.
60. Giomi L, Bowick MJ, Mishra P, Sknepnek R, Cristina Marchetti M. Defect dynamics in active nematics. Philos Trans A Math Phys Eng Sci. 2014;372(2029).